LAWRENCE
LIVERMORE
NATIONAL
LABORATORY

UCRL-TR-228924

Optimized performance for neutron interrogation to detect SNM

D. R. Slaughter, S. J. Asztalos, P. J. Biltoft, J. A. Church, M.-A. Descalle, J. M. Hall, T. C. Luu, D. R. Manatt, G. J. Mauger, E. B. Norman, D. C. Petersen, J. A. Pruet, S. G. Prussin

March 12, 2007

Disclaimer

This work performed under the auspices of the U.S. Department of Energy by Lawrence Livermore National Laboratory under Contract DE-AC52-07NA27344.

Summary

A program of simulations and validating experiments was utilized to evaluate a concept for neutron interrogation of commercial cargo containers that would reliably detect special nuclear material (SNM). The goals were to develop an interrogation system capable of detecting a 5 kg solid sphere of high-enriched uranium (HEU) even when deeply embedded in commercial cargo. Performance goals included a minimum detection probability, $P_d \geq 95\%$, a maximum occurrence of false positive indications, $P_{fA} \leq 0.001$, and maximum scan duration of $t \leq 1$ min. The conditions necessary to meet these goals were demonstrated in experimental measurements even when the SNM is deeply buried in any commercial cargo, and are projected to be met successfully in the most challenging cases of steel or hydrocarbons at areal density $\rho L \leq 150$ g/cm^2. Optimal performance was obtained with a collimated ($\Delta\theta=\pm 15^o$) neutron beam at energy $E_n = 7$ MeV produced by the D(d,n) reaction with the deuteron energy $E_d = 4$ MeV. Two fission product signatures are utilized to uniquely identify SNM, including delayed neutrons detected in a large array of polyethylene moderated ^{3}He proportional counters and high energy β-delayed fission product γ-radiation detected in a large array of 61x61x25 cm^3 plastic scintillators. The latter detectors are nearly blind to normal terrestrial background radiation by setting an energy threshold on the detection at $E_{min} \geq 3$ MeV.

Detection goals were attained with a low beam current (I_d=15-65 μA) source up to ρL=75 g/cm^2 utilizing long irradiations, T=30 sec, and long counting times, t=30-100 sec. Projecting to a higher beam current, $I_d \geq 600$ μA and larger detector array the detection and false alarm goals would be attained even with intervening cargo overburden as large as $\rho L \leq 150$ g/cm^2. The latter cargo thickness corresponds to 8 ft of hydrogenous or metallic cargo at the highest density allowed by the weight limit of the container. Simulations support the efficacy of this technique in the most challenging cases and experimental measurements are shown validating these predictions. Signal and background levels have been assessed and utilized to predict error rates due to false positive and false negative results. The laboratory system demonstrates the ability to detect HEU in amounts as small as m ≥ 250 g buried in the middle of a maximum density cargo and to do so with error rates that meet the goals given above. Higher beam current allows reliable SNM detection in shorter irradiation and/or counting times and with more challenging cargo threat scenarios.

Optimized performance for neutron interrogation to detect SNM

1. Introduction

A concept has been developed over the past several years to detect well-shielded special nuclear material (SNM) embedded in fully loaded cargo containers. It was first proposed by Norman and Prussin[1] and has often been referred to colloquially as the "nuclear car wash". The concept has been described in detail elsewhere[2-6] and consists of a brief irradiation of the cargo by a low-intensity and forward-directed beam of neutrons whose energies are in the range E_n=3-9 MeV. Some of the neutrons are thermalized in the cargo and induce fission in ^{235}U or ^{239}Pu that may be present. Fast neutrons also generate some fissions. After irradiation the cargo is surveyed by a large detector array to detect any fission product delayed radiation produced by SNM concealed in the cargo. Fission products decay by β-emission and some of those decays populate very high-energy states in the fission product daughter nuclei. Those high level states then emit delayed neutrons and γ-radiation.

Delayed fission product radiation is very distinctive. Delayed neutrons are not produced in the α or β decay of ordinary terrestrial background radiation and thus provide a unique signature for identification of fissionable material. They also penetrate non-hydrogenous or metallic cargos readily with minimal attenuation so that their escape probability is large for these cargo threats. They have been used for this purpose for several decades where the overlying material is either metallic or thin[7-11]. However, due to their low energies, of the order En~ 0.5 MeV, they do not readily penetrate hydrogenous material and do not escape thick cargo of liquids or agricultural products.

Fission product γ-radiation delayed fission product γ-radiation is nearly three decades more abundant than delayed neutron emission and about ~ 2% of the γ–radiation is produced at high energy, $E_\gamma \geq 3$ MeV, well above the maximum energy (2.6 MeV) of normal terrestrial background radiation. If a detector energy threshold is set above 2.6 MeV then the sensor is blind to terrestrial background radiation and to nearly all of the cargo activation products generated by the interrogating beam so that there are few interferences or false alarms when detection is based on delayed neutrons and/or delayed high-energy γ-rays. Setting a γ-ray detection threshold at E_{det} = 3 MeV results in rejection of 98% of the fission product γ-radiation but even then the residual high-energy γ-radiation is roughly a decade more abundant than the delayed neutrons[5]. The minimum γ-ray attenuation for all materials up to lead occurs in the energy range 2-6 MeV. Since the primary attenuation mechanism is by Compton scattering the attenuation is independent of Z and the mean free path is approximately ρ/μ=30 g/cm^2 in all commercial materials. High-energy β-delayed fission product γ-radiation escapes readily from all cargos and is easily detected with high probability.

Thus, delayed neutrons from β-decay of fission products escape readily from thick cargos of non-hydrogenous material and high-energy γ-radiation from β-

decay of fission products escapes readily from all thick cargos including hydrogenous materials. Both are unique signatures of fission and essential in reliable detection of SNM with low false alarm rates.

In spite of the uniqueness and penetrability of fission product radiation, all interrogation techniques are vulnerable to interferences such as those produced by activation of the cargo and by neutron spallation in the environment produced by high-energy cosmic radiation. Consequently, the details of detector design; collimation and energy spectra of the neutron source, timing and data processing all play key roles in the ultimate performance obtainable by neutron interrogation. The following sections will describe our choices as we optimize the design details and will offer a preliminary measurement of overall system performance. Finally, a projection of likely performance in the field with an upgraded version of this concept will indicate the ultimate limits of this technique.

2 Goals and performance evaluation

2.1 Evaluation criteria

Our primary goal in the work described here is the reliable detection of HEU. Specifically the goal is to reliably detect a 5 kg solid sphere of HEU embedded in any commercial cargo with low error rates, i.e. detection probability $P_d \geq 95\%$ and false positive probability $P_{fA} \leq .001$. The cargo screening technique described above could be applied as a primary screening technique where a high detection probability is required and where, due to a large flow of containers and the high cost of devaning, the rate of false positives must be low. In this application the time allowed for screening will be very short and the radiation dose to the cargo may be limited to low values. The same technique could also be applied as a secondary screening technique to resolve alarms generated by the primary screening employed at a portal. In this application the false positive rate must be very low and the detection probability equally as high as in primary screening. However, the time allotted to secondary screening may be considerably longer than in primary screening and limitation on radiation dose to the cargo may be relaxed substantially. Regardless of the ultimate application and even the CONOPS, evaluation of system performance must be carried out for each threat, i.e. for each combination of SNM target and intervening cargo or shield overburden. An appropriate figure of merit must be defined and each threat evaluated to determine the figure of merit. In this analysis we invoke the ROC (Receiver Operating Characteristic) curve, i.e. probability of detection vs. probability of false positive as a function of a detection threshold parameter. A ROC curve and/or figure of merit would then be determined for each threat.

In the following analysis it is assumed that detection is based on measuring a detector count rate or fitting of detector spectral and temporal decay data to obtain a radiation signature level. The level will always include backgrounds and/or interferences, and will contain fission signature data when a threat is actually present. Normal variation in background could produce false positive

indications or false negative indications. The former occurs when background counts randomly rise above the alarm threshold. The latter occurs if an SNM signal is masked by a random reduction in background so that the count total count rate does not rise above the alarm level.

We rarely know the statistical distribution of background levels in a portal environment where sources and shadows produced by environmental shields may be moving from time to time. In the absence of empirical knowledge it is generally assumed that the distribution is Gaussian and that will be the assumption here. The background count rate is assumed to have a Gaussian statistical distribution with known mean B and standard deviation σ. The error rates are then estimated as a function of the alarm level that is set. It is important to note that the standard deviation in the count rate includes the Poisson estimate, σ^2=N, for random radioactive decays. It also must include other systematic variations due to fluctuations in the cosmic ray spallation neutron background as cargo materials are moved about or as cargo materials provide a shadow shield for some of the detectable background. In general Poisson statistics will underestimate σ.

Estimation of error rates based on Gaussian counting statistics is illustrated by the figure below. An assumed distribution function for background count rate variations and SNM+background is shown. An alarm threshold, L, is set at some point above the mean background, B.

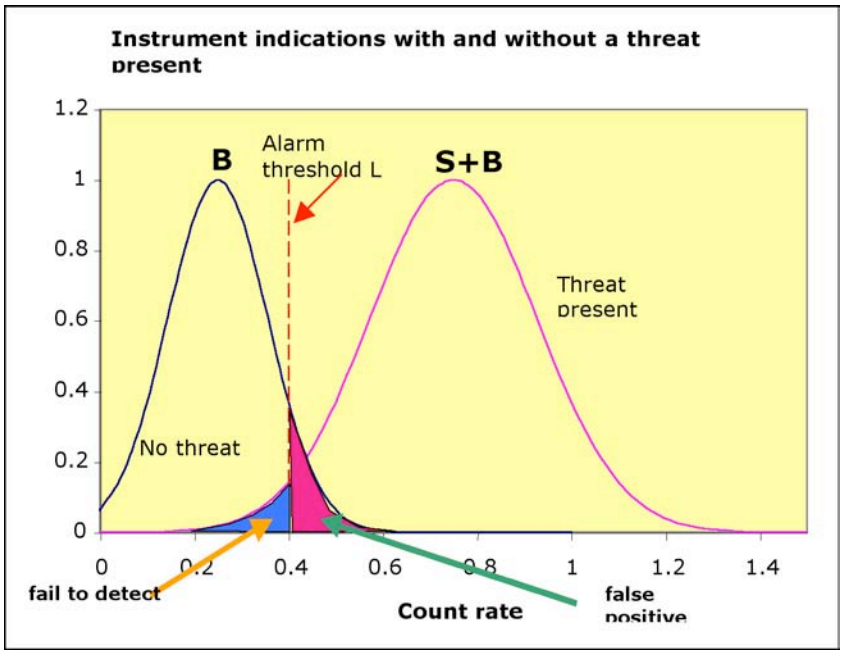

Figure 2.1-1 Illustration of Gaussian distributions for fission signature, S, and background, B.

False positives occur when random variations in background exceed the alarm threshold and false negatives occur when random variations in background depress the total rate and prevent the background plus SNM signal from rising above the alarm level, L. The probability of false negative, i.e. failure to detect $P_{fn}=1-P_d$ corresponds to the blue shaded area in the illustration. The probability of false positive, i.e. false alarm, P_{fA} corresponds to the red shaded area in the illustration. Thus, with the assumption of Gaussian statistics the error rates depend only on the background, B, signal S, standard deviation, σ, and the discriminator level L. In the Gaussian assumption the error rates are given by:

$$P_d = \frac{1}{2}\left[1 + erf\left(\frac{S + B - L}{\sqrt{2}\sigma}\right)\right] \qquad 2.1\text{-}1$$

$$P_{fA} = \frac{1}{2}\left[1 - erf\left(\frac{L - B}{\sqrt{2}\sigma}\right)\right] \qquad 2.1\text{-}2$$

Note that for simple situations where the background is due only to random decays, not effected by beam-induced activation, and there is no movement of the source or shielding then the counting statistics are well described by the Poisson distribution, i.e. $\sigma^2=B$ and the Gaussian distribution is usually a reliable description. In general there may be systematic variations in background that force $\sigma^2 > B$. Whether or not Poisson statistics apply, a curve showing the error rates as a function of L is the ROC curve and is used to assess system performance. To simplify the analysis we define a figure of merit, F_s for the signal strength and background factor F_b for the interfering background.

$$F_s \equiv \frac{S}{\sigma} \qquad 2.1\text{-}3$$

$$F_b \equiv \frac{B}{\sigma} \qquad 2.1\text{-}4$$

Then a generic ROC curve can be constructed from these two factors.

$$P_d = \frac{1}{2}\left[1 + erf\left(\frac{F_s + F_b - \frac{L}{\sigma}}{\sqrt{2}}\right)\right] \qquad 2.1\text{-}5$$

$$P_{fA} = \frac{1}{2}\left[1 - erf\left(\frac{\frac{L}{\sigma} - F_b}{\sqrt{2}}\right)\right] \qquad 2.1\text{-}6$$

We note that in those cases described by Poisson statistics $F_b=\sigma$, and otherwise $F_b < \sigma$. Intuitively, it is clear that the value of B alone does not determine the error rate and that F_b is an unimportant parameter in this evaluation. This is demonstrated in the two figures below where ROC curves are estimated for $F_b=10$ and $F_b=100$ and they are found to be nearly identical.

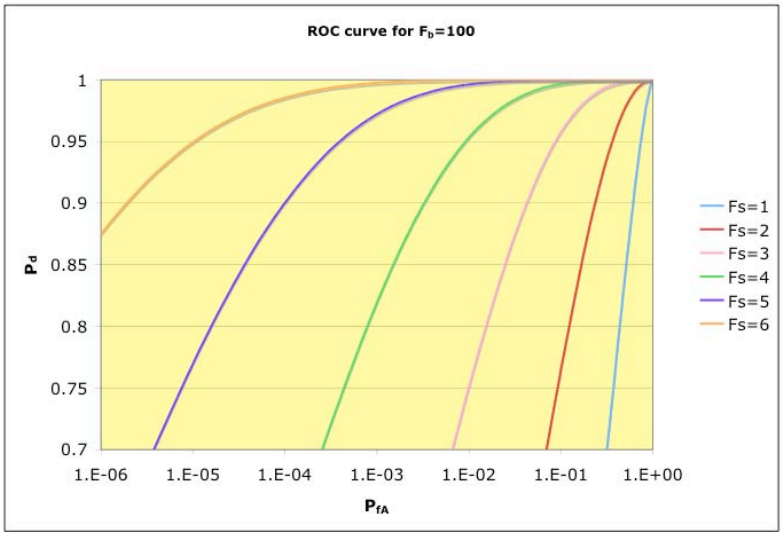

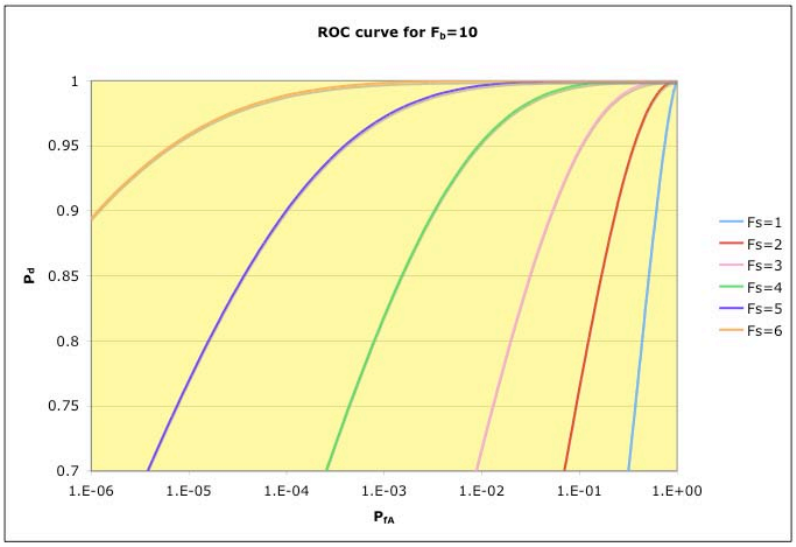

Figure 2-2 Generic ROC curves for F_s=1 to 6 and for two different background levels.

Comparing the ROC curves it is clear that large variations in F_b have no observable effect on error rates and this parameter is unimportant. It will not be considered further.

2.2 Performance goals

The primary conclusion from the figures is that the range $F_s = 1$ to $F_s = 6$ spans an enormous range in error rates. Very high rates of false positives and false negatives are predicted for $F_s \leq 2$. Very low error rates are predicted for $F_s \geq 5$. Moderately low error rates are predicted in the range $F_s = 3$-4 and very satisfactory performance is predicted at $F_s = 5$. The following analyses will utilize the figure of merit defined in Eq. 2.1-3 and the system is predicted to perform well against any cargo threats where $F_s \geq 5$ and marginally adequate for threats where $F_s \geq 3$.

The laboratory prototype evaluated in the measurements generates a background count rate B~ 50 Hz per detector and the experimental evaluations typically deployed four detectors. The experimental validations were carried out utilizing a T=30 sec irradiation followed by counting for up to t=100 sec after the end of irradiation. Given the observed half-lives of the important fission product γ-ray emitters a counting interval of t=30 sec is long enough to detect all of the important fission product decays.

In the experiments four detectors produce 6000 background counts in 30 sec. Heretofore, it was found that systematic variations in background[12] add 10% to the Poisson variations so that σ~ 85 counts. The previous section established that the reliability goals are met when $F_s \geq 5$ or when the minimum number of detected fission events is $N_{det} \geq 430$. This requirement on the minimum number of fissions actually detected then forms the basis for the specifications on the neutron source and the detector array.

3. Optimization of parameters

3.1 Incident neutron spectrum and source strength

3.1.1 Sealed sources

Neutron sources come in many forms. Readily available sources include 2.5 MeV neutrons generated by the D(d,n) reaction in a sealed electrostatic accelerator with maximum voltage in the neighborhood of E_d ~ 200 kV. Commercially available units have isotropic emission with total output up to $1x10^9$ n/s. In the absence of attenuation this source can produce a neutron flux at R=2.5 m up to $\Phi \leq 1.3x10^3$ n/cm^{2}sec. Similarly, 14 MeV neutrons are produced in sealed source tubes by the T(d,n) reaction. At the same current and voltage these sources can produce up to $1x10^{11}$ n/s, or $\Phi \leq 1.3x10^5$ n/cm^{2}sec at R=2.5 m. Rarely do the sealed source tubes produce output more than about half of the maximum specified. Plasma sources have increased the neutron yield from the D(d,n) and

T(d,n) reaction about one decade and may be extendable to higher output but these units are not available commercially.

3.1.2 RFQ accelerators

Neutron sources can be generated by the ^{6}Li(p,n) reaction at low energies. A beam of protons is accelerated in an RFQ to E_p ~ 2 MeV. The neutron production reaction has a threshold energy of E_{min}=1.89 MeV so that the proton beam produces neutrons at E_n ~ 60 keV and reaction kinematics constrain the neutrons to a tightly collimated forward beam, reducing neutron dose in the environment away from the forward direction and producing much larger flux on target than for an isotropic source of the same total output. At low energies such a neutron source does not penetrate thick hydrogenous cargo but may be efficacious for non-hydrogenous cargo.

Alternatively, neutrons can be generated by the D(d,n) reaction in a deuteron beam accelerated to E_d=3-6 MeV. If a gas target of deuterium is employed and is thick enough to stop the beam then neutrons are produced with energies in the range 3-9 MeV depending on the deuteron beam energy as shown in the figure below.

.

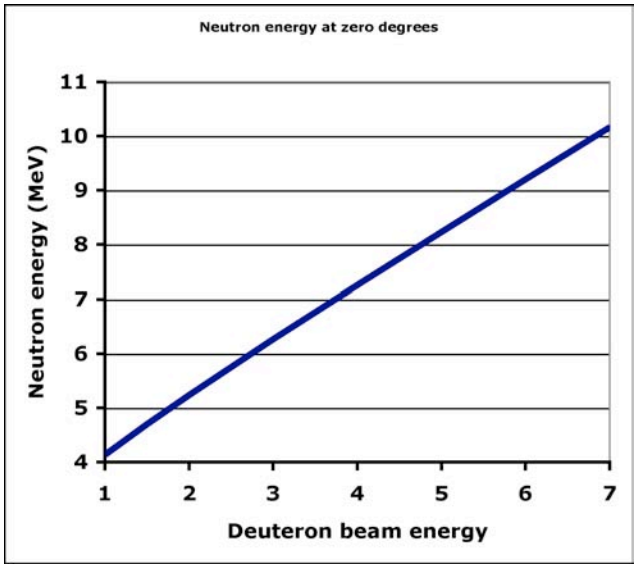

Figure 3.1.2-1 Neutron energy vs. deuteron beam energy.

Here too the reaction kinematics and the cross section produce a beam highly peaked in the forward direction. At E_d=4 MeV the half width of the neutron beam is $\Delta\theta \leq \pm 15^o$. This can be seen in the figure below.

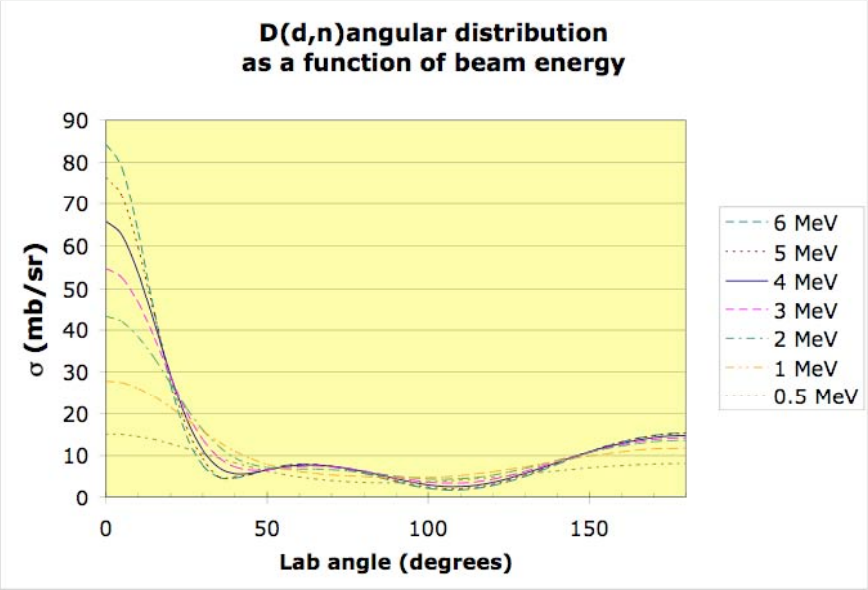

Figure 3.1.2-2 Angular distribution of the D(d,n) for several beam energies.

The yield of D(d,n) sources increases dramatically with deuteron beam energy as shown in the figure below.

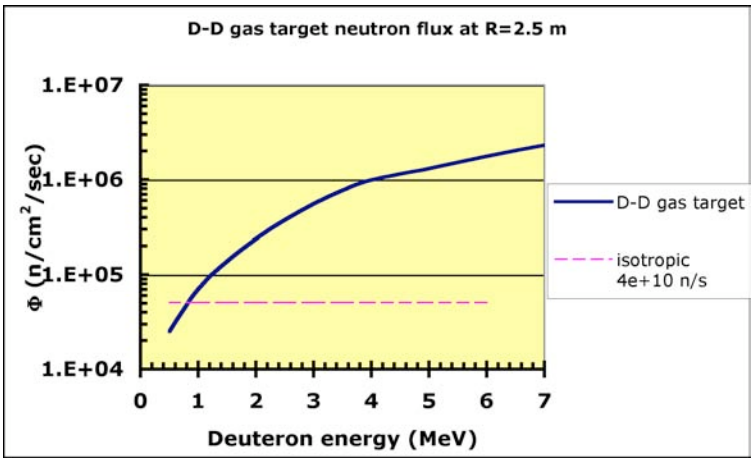

Figure 3.1.2-3 Yield of D(d,n) source vs. deuteron beam energy for beam current I_d=100 μA.

Deuteron beam current $I_d = 100$ μA can readily generate a neutron flux $\Phi \leq 2x10^6$ n/cm^{2}sec at R=2.5 m in the absence of beam attenuation. The flux on target produced by an RFQ is substantially more than is available from isotropic sealed source tubes whose flux is shown in the figure by the dashed line. It is directed forward so that the shielding requirements are reduced. Only modest increases in neutron flux are achievable by increasing the deuteron energy above $E_d \sim 4$ MeV. Commercially available RFQ accelerators provide beam currents up to $I_d = 400$ μA and manufacturers have the ability to provide machines up to $I_d \sim 1$ mA so that the neutron flux at R=2.5 m can be increased to $\Phi \leq 2x10^7$ n/cm^{2}sec.

3.1.3 Neutron energy

Neutrons penetrate most materials readily though substantial attenuation occurs in thick cargos of hydrogenous material. In all cases the penetration increases dramatically with neutron energy. This is seen in the figure below.

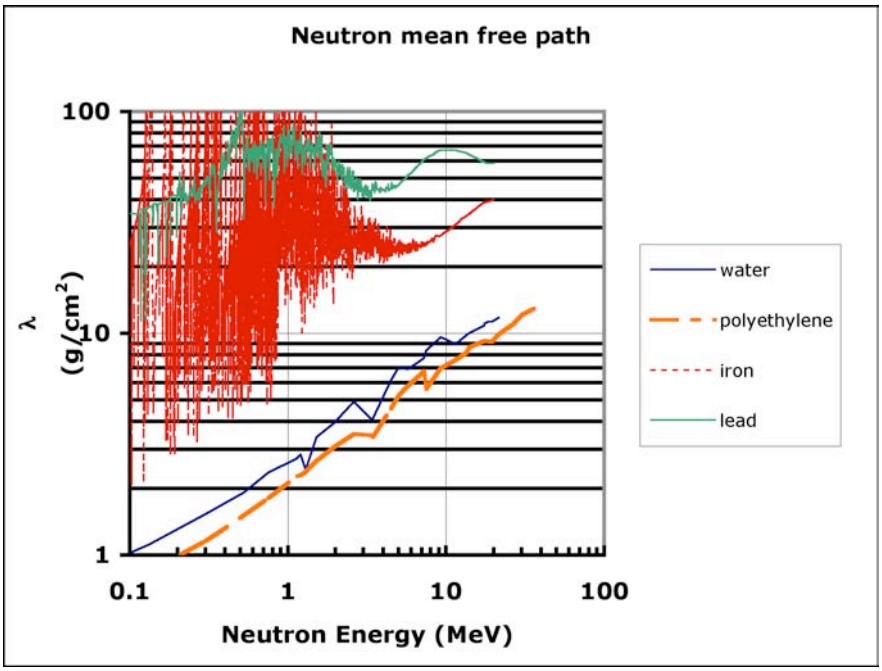

Figure 3.1.3-1 Neutron mean free path vs. energy in common commercial cargo materials.

The figure shows that neutron attenuation is relatively small in metals at all energies of interest and so beam energy is not critical for those cargo threats. However, hydrogenous cargo is strongly attenuating and beam energies less than $E_n \leq 3$ MeV provide very poor penetration. In general neutron interrogation energies in the range E_n=6-9 MeV provide optimum penetration without introducing interferences due to beam-induced activation.

At the upper end of the energy range introduction of interferences by neutron activation can reduce detection sensitivity and increase false positive rates. The most important of the interfering reactions for this technique is the $^{16}O(n,p)^{16}N$

reaction. The ^{16}N produced has a 7.1 sec half-life and a primary γ-ray at E_γ=6.1 MeV and thus has characteristics within the range otherwise unique to fission products. Its reaction threshold is E_n=10.25 MeV and this puts an upper limit on useful neutron interrogation energy.

There are other potential interferences due to activation of cargo materials. The table below lists the nuclides that produce high-energy γ-radiation. For comparison they are listed according to their importance, which is proportional to their specific activity. The prioritized list is indicated in the table below.

Table 3.1.3-2 Neutron activation products that produce high-energy γ-radiation with half-lives less than 10 min.

Z	Target	(%)	Reaction	Threshold (MeV)	Product	Half-life (sec)	Y_γ	A_γ/M
8	^{16}O	99.8	(n,p)	11	^{16}N	7.1	7.2E-01	1.2E-04
9	^{19}F	100	(n,α)	2	^{16}N	7.1	7.2E-01	6.4E-05
5	^{11}B	80	(n,p)	11.8	^{11}Be	13.8	1.1E-01	1.3E-06
14	^{30}Si	3.1	(n,p)	8.3	^{30}Al	3.68	3.4E-01	9.0E-07
7	^{15}N	0.37	(n,p)	10.1	^{15}C	2.45	6.3E-01	5.6E-07
12	^{26}Mg	11	(n,p)	9	^{26}Na	1.07	4.0E-03	2.3E-07
17	^{37}Cl	24.2	(n,α)	6.97	^{34}P	12.4	1.7E-02	1.9E-07
8	^{18}O	0.2	(n,α)	7.7	^{15}C	2.45	6.3E-01	1.0E-07
40	^{96}Zr	2.8	(n,p)	7	^{96}Y	9.6	1.4E+00	4.9E-08
20	^{48}Ca	0.187	(n,γ)	0	^{49}Ca	523.2	1.0E+00	4.1E-08
16	^{34}S	4.2	(n,p)	4.7	^{34}P	47	1.7E-02	2.1E-08
11	^{23}Na	100	(n,α)	6	^{20}F	11	8.0E-05	1.7E-08
24	^{54}Cr	2.38	(n,p)	7.5	^{54}V	49.8	1.6E-01	6.1E-09

Isotopic abundances are given for each target nucleus and neutron energy thresholds are given for each reaction. Half-lives of the reaction products are considered only out to $T_{½} \leq 10$ min since long-lived species are readily distinguished from fission products. Total yield of γ-radiation at energies above $E_\gamma \geq 3$ MeV is given as well and then a figure of importance is calculated to provide an index for prioritizing each interference. The importance, shown in the right-most column is given by the specific initial activity (γ-ray emission rate per gram) for unit neutron fluence.

$$\frac{A_\gamma}{M} = \frac{\varepsilon \sigma Y_\gamma}{T_{1/2}} \qquad 3.1.3\text{-}1$$

Where ε is the isotopic abundance of the reacting nuclide, σ the reaction cross-section at E_n = 10 MeV, Y_γ the yield of γ-radiation above $E_\gamma \geq 3$ MeV, and $T_{1/2}$ the half-life of the interfering species.

Examination of the table shows that ^{16}N production by oxygen activation or from low energy activation of ^{19}F is, by far, the most important interference. Oxygen or boron activation is eliminated when the beam energy is less than $E_n \leq 10$ MeV. On the other hand ^{19}F activation has a very low threshold and reducing the beam energy to accommodate it would be impractical so that this interference is not readily suppressed in cargo containing fluorine. Beyond fluorine activation there are several others that may be introduced as beam energy is increased but their importance, as indicated by Eq. 3.1.3-1, is 3-5 decades less than ^{19}F and for our purposes those potential interferences do not guide our choice of beam energy. Nevertheless, we note that neutron beam energies below $E_n \leq 7$ MeV do not activate ^{30}Si, ^{26}Mg, ^{18}O, or ^{54}Cr. Since reduction of the maximum neutron beam energy from E_n=9 MeV to E_n= 7 MeV results in less than 20% reduction in cargo attenuation coefficient we judge this a small penalty to reduce the number of interferences. Of course it is important to note that when cargos are many mean free paths thick then a 20% reduction in attenuation coefficient becomes important. For example, when $\rho L \geq 100$ g/cm^2 the thickness is L=8-10 λ so that a 20% increase in attenuation coefficient results in a ~ 10X reduction in the intensity on target.

Fluorine remains a concern as it occurs in ~ 5 % of cargo shipments[13] and can produce a significant interference with fission product detection. Nevertheless, its strong single γ-ray at E_γ=6.1 MeV and its distinctive half-life, $T_{½}$=7.1 sec which is distinct from all of the fission product groups, make this interference relatively easy to identify and suppress in the analysis. An automated procedure has been developed to: a) identify ^{16}N radiation by its characteristic pulse height spectrum of the mono-energetic γ-ray, and distinct half-life, and b) subtract the ^{16}N contribution from the pulse height and temporal data. Recognition and suppression of ^{16}N signals in the data analysis is facilitated by the mono-energetic spectral and unique half-life decay characteristics of this interference that are clearly distinct from characteristics of fission product β-delayed γ-radiation.

Final resolution of the optimal choice for neutron beam energy is based on predicted fission rate when a target sample of 5 kg HEU is embedded deeply in either wood or steel cargo. Monte Carlo simulations have been carried out to find the optimal interrogation energy for wood, aluminum, and steel cargo. Results are shown in the following three figures.

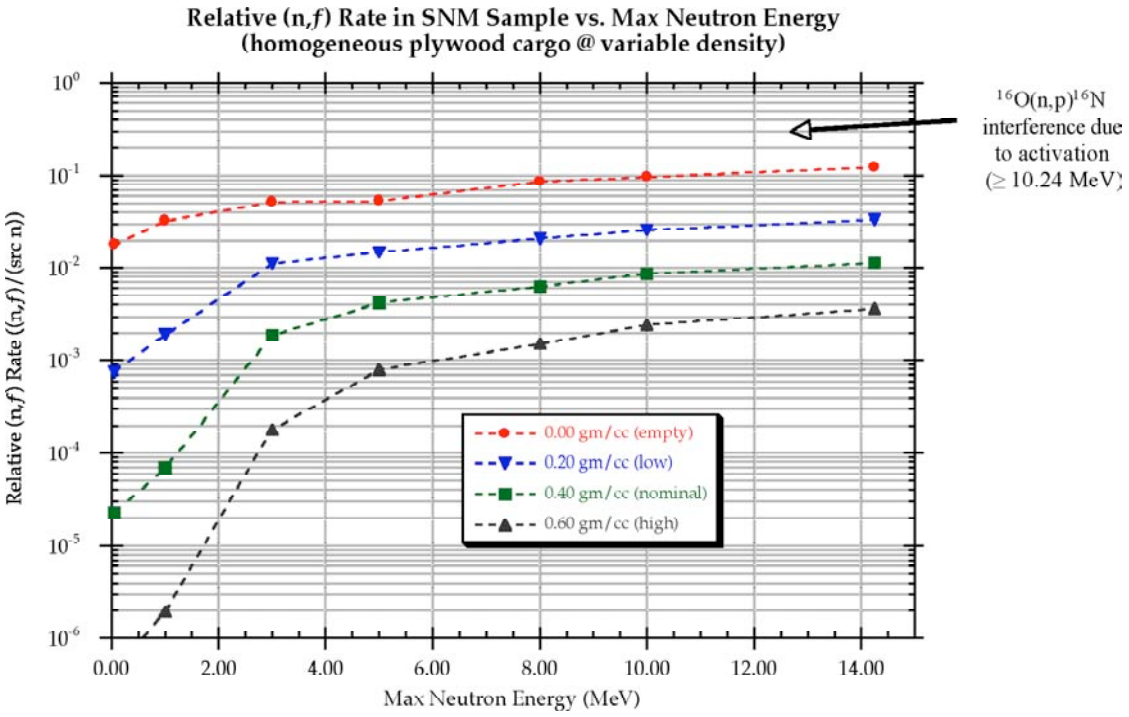
Relative (n,f) Rate in SNM Sample vs. Max Neutron Energy
(homogeneous plywood cargo @ variable density)
Relative (n,f) Rate ((n,f)/(src n))
Max Neutron Energy (MeV)
0.00 gm/cc (empty)
0.20 gm/cc (low)
0.40 gm/cc (nominal)
0.60 gm/cc (high)
16O(n,p)16N
interference due
to activation
(≥ 10.24 MeV)

(a)

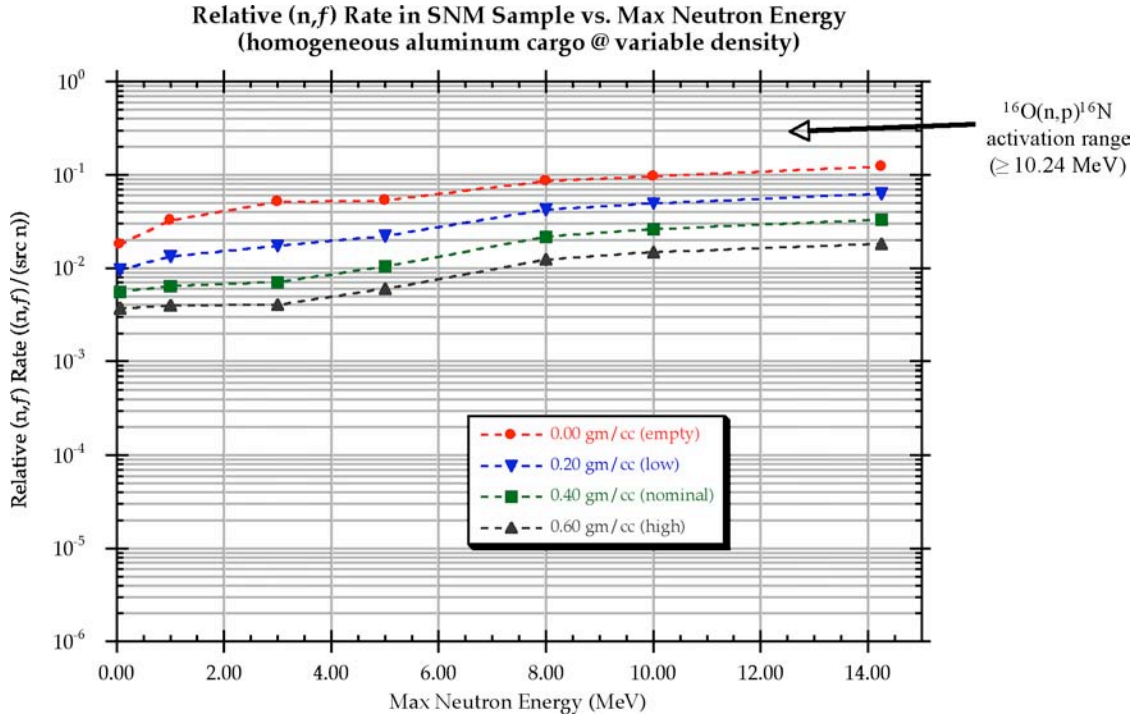
Relative (n,f) Rate in SNM Sample vs. Max Neutron Energy
(homogeneous aluminum cargo @ variable density)
Relative (n,f) Rate ((n,f)/(src n))
Max Neutron Energy (MeV)
0.00 gm/cc (empty)
0.20 gm/cc (low)
0.40 gm/cc (nominal)
0.60 gm/cc (high)
16O(n,p)16N
activation range
(≥ 10.24 MeV)

(b)

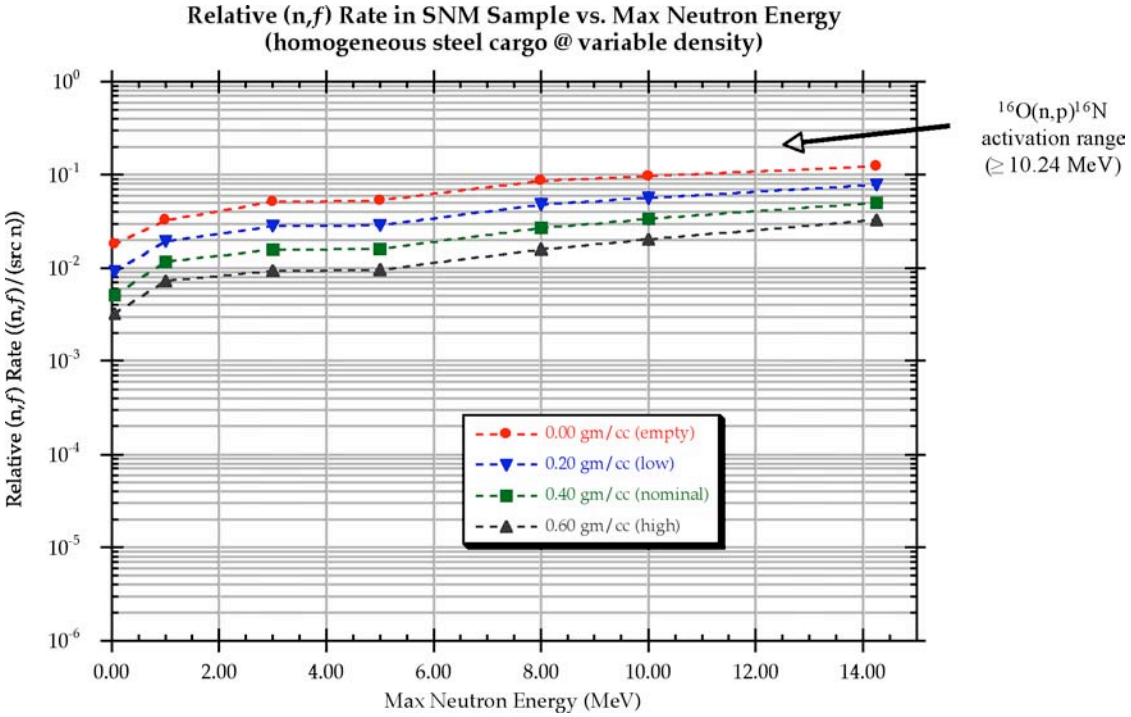

(c)

Figure 3.1.3-2 Predicted fission rate vs. neutron beam energy. a) wood cargo, b) aluminum cargo, c) steel cargo[14].

The optimum choice for the deuteron beam energy is then E_d=4 MeV and the neutron spectra emitted from the throat of the polyethylene collimator have been determined by simulations. The proof of concept (POC) constructed at LLNL employs an E_d = 4 MeV deuteron beam. After losing ΔE=0.725 MeV in the vacuum window, the beam enters a deuterium gas target at E_d=3.25 MeV and stops in the gas. Simulations have been utilized to estimate the neutron spectrum of this source and the result is shown in the figure below.

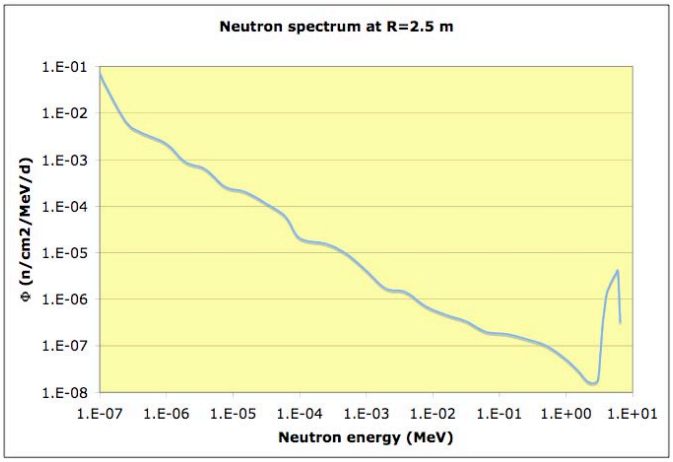

Figure 3.1.3-3 Energy spectrum of the unattenuated LLNL neutron source with its collimator in place.

The neutron beam is strongly altered by scattering as it penetrates the cargo as shown below.

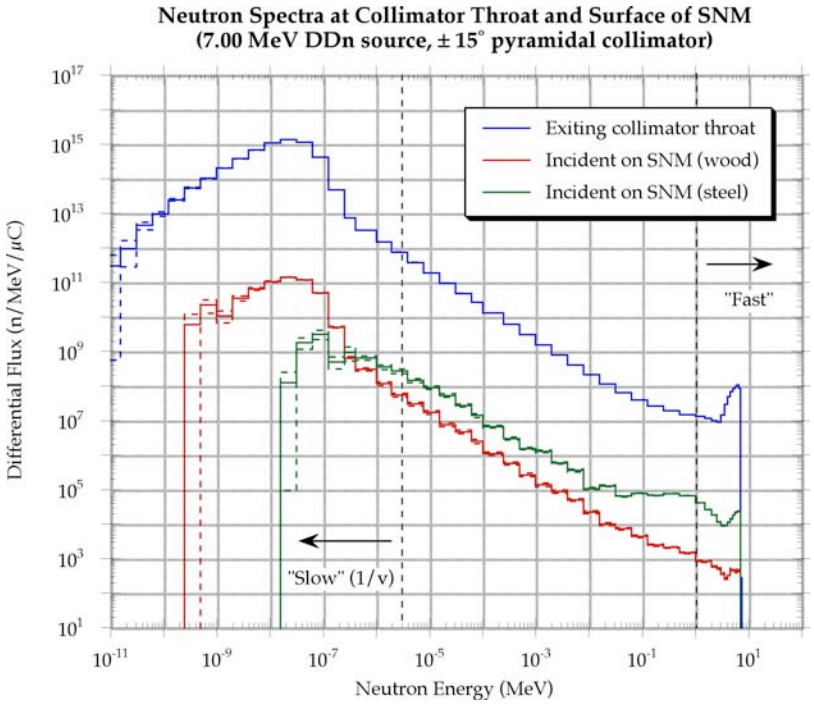

Figure 3.1.3-4 Energy spectrum of the attenuated beam after passing through thick (75 g/cm^2) wood and steel cargo[14].

Examination of the figure demonstrates that both wood and steel cargo attenuate the interrogating beam significantly. In addition, the steel cargo facilitates a large scattering escape probability that interferes with thermalizing the interrogation neutrons and thermal fission is less likely than fast fission in this environment. While wood media attenuate the fast neutrons more severely, this environment facilitates thermalization so that the high thermal fission cross-section enhances the fission rate.

Penetration of this source could be improved by increasing the deuteron energy from $E_d = 4$ MeV to $E_d = 5$ MeV or $E_d = 6$ MeV. The increase is associated with a longer and more expensive source and may not be cost effective as discussed earlier. Examination of Fig 3.1.3-1 shows that the benefit of this energy increase is only a factor of 2X intensity increase for SNM deeply embedded in wood cargo. Thus, the greater attenuation in wood at lower beam energies is largely offset by improved thermalization that increases the fission probability. The lower fission rate at lower neutron energy may be readily offset by doubling the detection efficiency and this is much less expensive than increasing the source energy.

LLNL has employed an E_d=4 MeV RFQ capable of $I_d \leq 100$ μA. Its parameters were driven by cost rather than optimization. Its length is approximately L=5 m and it was obtained from a commercial supplier. It is shown below. Its operation has been reliable and not overly complex.

Figure3.1.3-5 RFQ accelerator utilized as the neutron source.

3.1.4 Optimum neutron energy

Summarizing the discussion above it is clear that the highest neutron energy provides the best penetration of thick cargos. However, an important interference due to activation in oxygen can be suppressed only when the maximum neutron energy is $E_n \leq 10$ MeV. It is important to have a wide spread in beam energy to provide the highest thermal neutron flux in those cargos where moderation is minimal. This is provided by stopping the deuteron beam in the neutron production target and by employing collimation that scatters some of the beam to lower energies. Thus a spectrum of neutrons from the source nominally spanning the range E_n = 3-7 MeV is optimal.

3.2 Accelerator beam current

3.2.1 Neutron flux required

Deuteron beam currents utilized in LLNL measurements have typically been in the range I_d = 15-65 μA. Commercially available RFQs readily provide beam currents $I_d \leq 400$ μA and could be produced at currents up to $I_d \leq 1$ mA. The important cargo threats vary over a wide range in composition and density. While normal cargos tend toward low densities[13], i.e. ρ~0.1-0.3 g/cm^3, the goal here is to address the most challenging threat scenarios as those are most likely to be the alarming cases generated by primary screening and sent to secondary for resolution. At the high end of the threat range is wood cargo at thickness ρL=150 g/cm^2.

A previous section established that for the conditions under which validating measurements were carried out, with a γ-ray counting period t=30 sec in four detector modules, the reliability goals were met only if the number of fission product decays detected in that period was $N_{det} \geq 430$. In the case of wood cargos only fission product γ-radiation needs consideration, as delayed neutrons will not escape the cargo. Simple estimates of error rates in detection, both false positive and false negative, indicate that the high-energy γ-ray fluence exiting the cargo and incident on the detector after a brief irradiation must be at least:

$$\Phi_\gamma t = \frac{N_{\det}}{\varepsilon A} \qquad 3.2.1\text{-}1$$

$$N_{\det} = A\varepsilon \frac{N_{fiss} Y_\gamma \beta_t}{4\pi R^2} e^{-\left(\frac{\mu}{\rho}\right)\rho L} \qquad 3.2.1\text{-}2$$

Where Φ_γ is the γ-ray flux (γ/cm^2/sec) at the detector which is R=2.5 m from the SNM, t is the duration of counting. N_{det} is the number of fission product high-energy γ-ray events that must be recorded at the detector location and above the energy cutoff in order to meet the error rate goals $P_d \geq 0.95$ and $P_{fA} \leq 0.001$. ε is the detection efficiency for high-energy γ-rays (ε=0.3); and A is the frontal area of the detectors (A=1.5x10^4 cm^2). N_{det} drives the number of fissions required where Y_γ =0.13 [5] is the number of high-energy β-delayed γ-rays produced per fission,

and β_t is the fraction of those emitted during the counting time, t. N_{fiss} is the number of fissions generated by the beam. Of course the fraction of decays accessible to detection is given by:

$$\beta_t = 1 - e^{-\lambda t} \qquad 3.2.1\text{-}3$$

where λ corresponds to the mean half life of fission product decays, $T_{½} = 22$ sec observed for the decay of high-energy fission product γ-rays[1], and t=30 sec is the normal counting period for the experiments described here, so that β_t=0.6. For the conditions given $\Phi t \geq 0.1\ \gamma/cm^2$ at R=2.5 m, the detector location. Nearly all cargos have the same γ-ray attenuation coefficient, μ/ρ=0.034 cm^2/g at the relevant energies. For a cargo thickness ρL=75 g/cm^2 the γ-ray exponential attenuation is f=0.078. Then the minimum number of fissions needed is $N_{fiss} \geq 1.3 \times 10^7$. <u>This drives the beam current requirement</u>.

Below is the result of a simulation for wood cargo at full thickness with the SNM target at the container centerline. The data shown includes detailed modeling of the neutron source with a gas target as well as beam transport in the cargo.

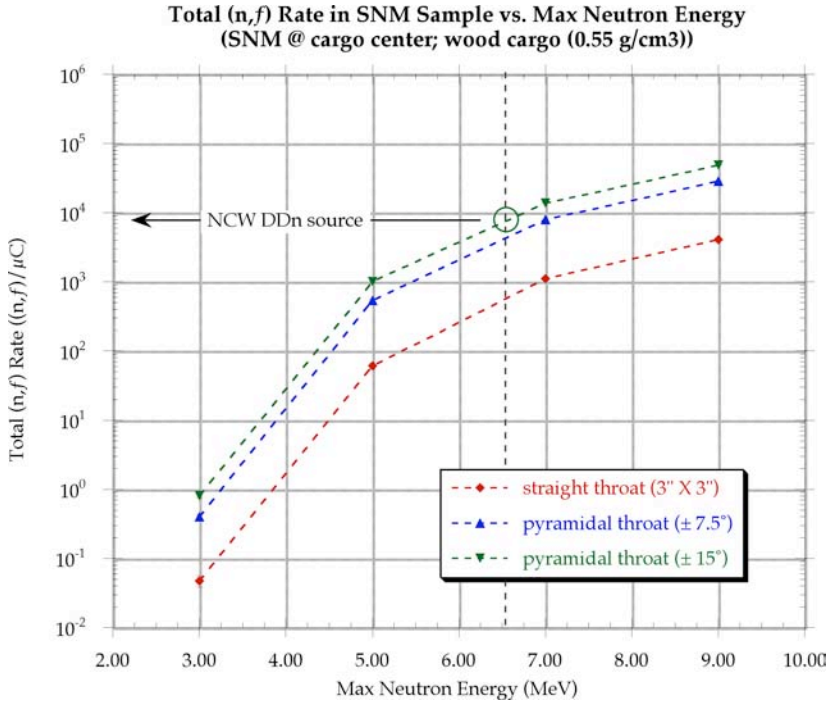

Figure 3.2.1-1 Simulated fission rate vs. neutron energy for several collimator configurations[14].

From the figure we see that, even with an open collimator the 7 MeV neutron source produces only ~ 9×10^3 fission/μC so that the minimum detectable fissions will require a total beam incident on generator target of q ≥ 1.4 mC. If the irradiation were limited to T=1 sec then the beam requirement is $I_d \geq 1.4$ mA.

That capability is probably attainable in commercial systems but exceeds the capability of routinely delivered systems. If the irradiation could be extended to T=2-3 sec then the beam current is reduced correspondingly to I_d=0.5-0.7 mA.

3.2.2 Beam current for gas target

A 4 MeV deuteron beam stopping in a D_2 gas target will traverse a useful target thickness of approximately $\rho L \geq 0.0046$ g/cm^2 which is L~25 cm at STP. The gas target effectively places ~ 1.4×10^{21} deuterium atoms/cm^2 in the beam path. It will generate a neutron fluence on axis at R=2.5 m of $\Phi_n T = 1 \times 10^7$ n/cm^2/mC. The previous section established the minimum irradiation fluence required $q \geq 1.4$ mC to produce enough fissions for reliable detection of SNM with acceptably low error rates for a threat based on 5 kg HEU deeply buried in any cargo material. Time limits for irradiation are based on limited time available for container scanning. If a 40 ft container passes through the portal at a mean velocity <v>= 20 cm/sec it will complete the scan in one minute. As will be shown later, the irradiated volume is exposed to a beam with lateral extent ~ 100 cm. At this velocity any cargo element is exposed to the beam for only T=5 sec. It is also shown later that the largest number of detected counts would accrue when the irradiation has a 50% duty cycle. Consequently, the beam will be on only half the time and the net irradiation to any volume in the container will have T~ 2.5 sec. Of course a longer irradiation is possible if the total scan time is allowed to exceed one minute. Given the requirements of $q \geq 1.4$ mC beam and an irradiation time of T ~ 2.5 sec the peak beam current must be $I_d \geq 0.6$ mA.

A picture of the LLNL gas target is shown below.

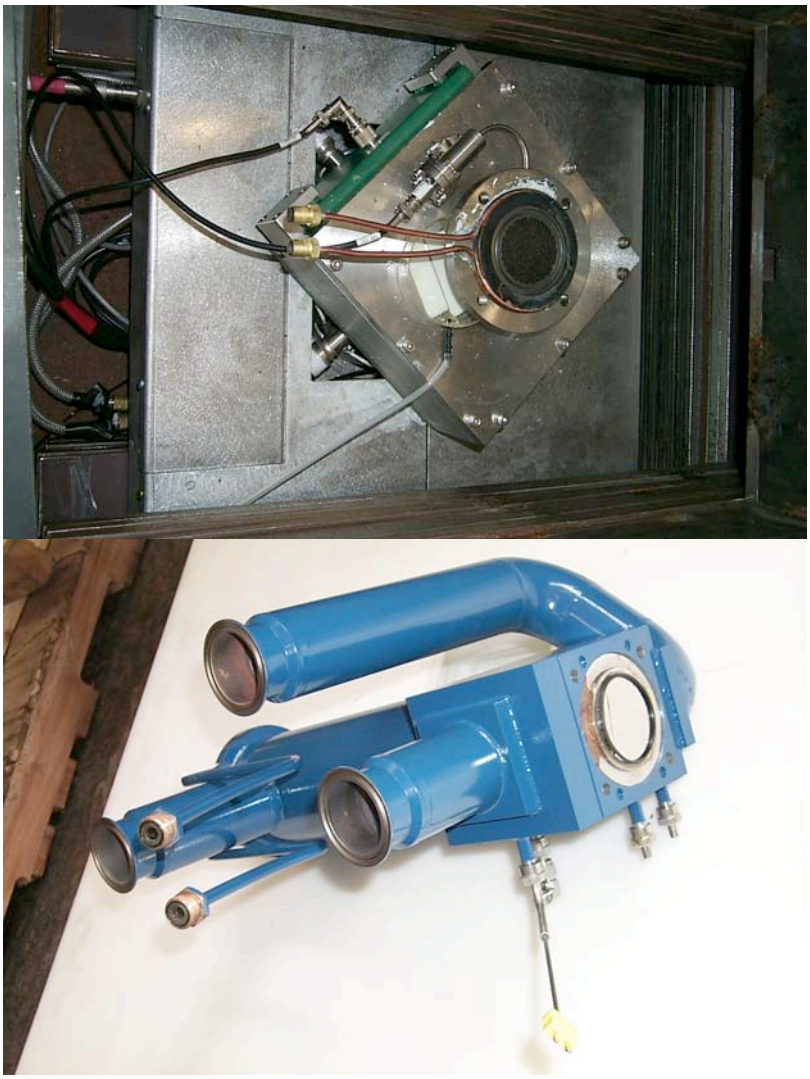

Figure 3.2.2-1 Neutron generator gas target. Upper photo shows Mo window and window cooling loop. Lower photo shows gas target assembly prior to installation.

3.2.3 Beam current for solid or liquid target

Several alternatives to the gas target have been considered including a carbon target that produces neutrons by the $^{12}C(d,n)^{13}N$ reaction, D(d,n) in a Ti matrix, and D(d,n) in heavy water, i.e. D_2O. The first reaction in a graphite target provides a mechanically robust target able to withstand high temperatures but produces a low neutron yield. In addition, the low energy (E_n=1-3 MeV) neutrons have poor penetration and are distributed isotropically producing a low flux.

The D(d,n) reaction in a Ti matrix is a viable candidate that eliminates the vacuum window at the target entrance and thus can withstand high beam currents more readily than the gas target. Ti can, when vapor deposited on a

metal substrate, hold up to 2.5 deuterium atoms per Ti atom. However, the Ti matrix removes energy from the beam more rapidly than D_2 gas and thus the effective thickness of the target is less. In Ti matrix a 4 MeV deuteron has a range of $\rho L=0.014$ g/cm^2 which places only ~ $4x10^{20}$ deuterium atoms/cm^2 in the beam path even at 2.5 deuterons per Ti in the matrix. That is only about one quarter the target mass of the gas target. Similarly, the range of deuterons in heavy water, D_2O, is approximately $\rho L=0.0075$ g/cm^2 and the target density is ~ $5x10^{20}$ deuterium atoms/cm^2, again about one third that of the gas target.

Overall, the liquid and solid targets are compact and mechanically rugged. They are a great deal cheaper to fabricate and maintain than the gas target. The solid targets can withstand fairly large beam currents though high temperatures will result in diffusion of the deuterium target out of the matrix. However, the beam current must be at least 3X-4X larger to produce a given neutron output from a solid or liquid target as compared to the gas target. The additional cost in the accelerator is likely to offset the savings in target maintenance and is not optimal.

3.3 Source collimation

The neutron output from the D(d,n) reaction at $E_d = 4$ MeV is highly peaked in the forward direction. This was illustrated in an earlier figure. Simulations have been utilized to estimate the angular width of the beam as a function of neutron energy. It is important to notice that collimation scatters some of the beam into the forward direction, but the scattering contributes to the low energy part of the source spectrum. Thus, the angular width has strong energy dependence. Scattering in the collimator can enhance the thermal neutron flux and increase the fission rate while tighter collimation reduces the total number of neutrons entering the cargo.

On the other hand even a parallel beam is scattered in all cargo materials so that it becomes spatially broad at depth in the local materials. Even a tightly collimated beam illuminates a roughly 100 cm wide zone within the cargo volume. The figure below shows the extent of spreading for a pencil beam.

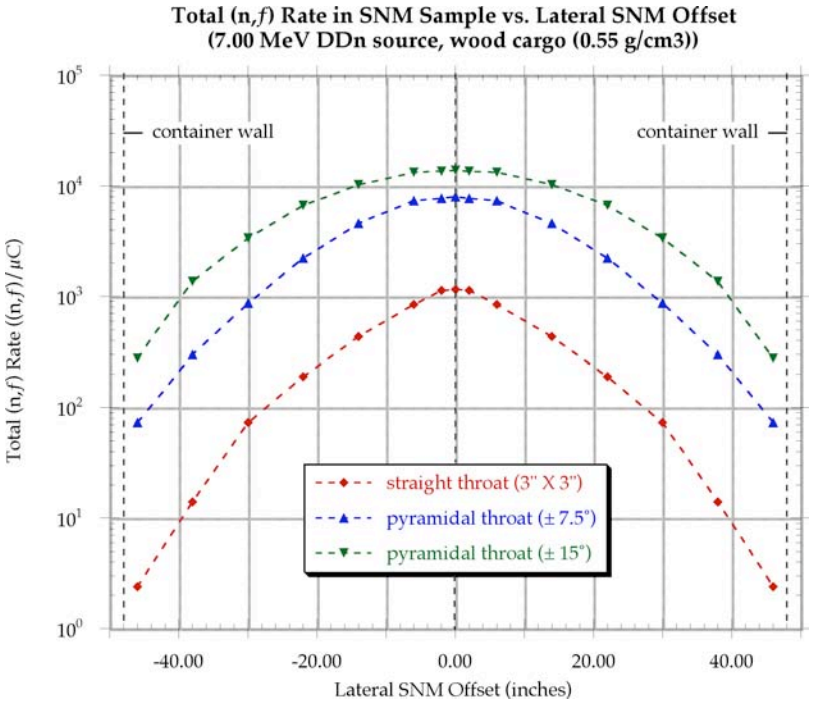

Figure 3.3-1 Lateral spatial distribution of neutron beam in cargo[14].

The LLNL neutron collimator is shown in the photographs below.

Figure 3.3-2 Neutron collimator at various stages of assembly. Top: gas target enclosed by steel collimator plates, top view. Middle: assembly of steel plates for interior collimation, side view. Bottom: polyethylene front collimator, top view looking down toward gas target vacuum connection.

As shown in the photos the inner collimator consists of steel plates that provide a high-density attenuation medium for side and backward directed source neutrons. The steel serves as a moderator, reducing the source neutron energy toward thermal where polyethylene provides strong absorption. The forward collimator consists of polyethylene sheets 5.1 cm thick that define a rectangular beam limited to $\Delta\theta = \pm 15^{o}$ from beam centerline. Dimensions for the collimator are shown in the figure below, given in inches.

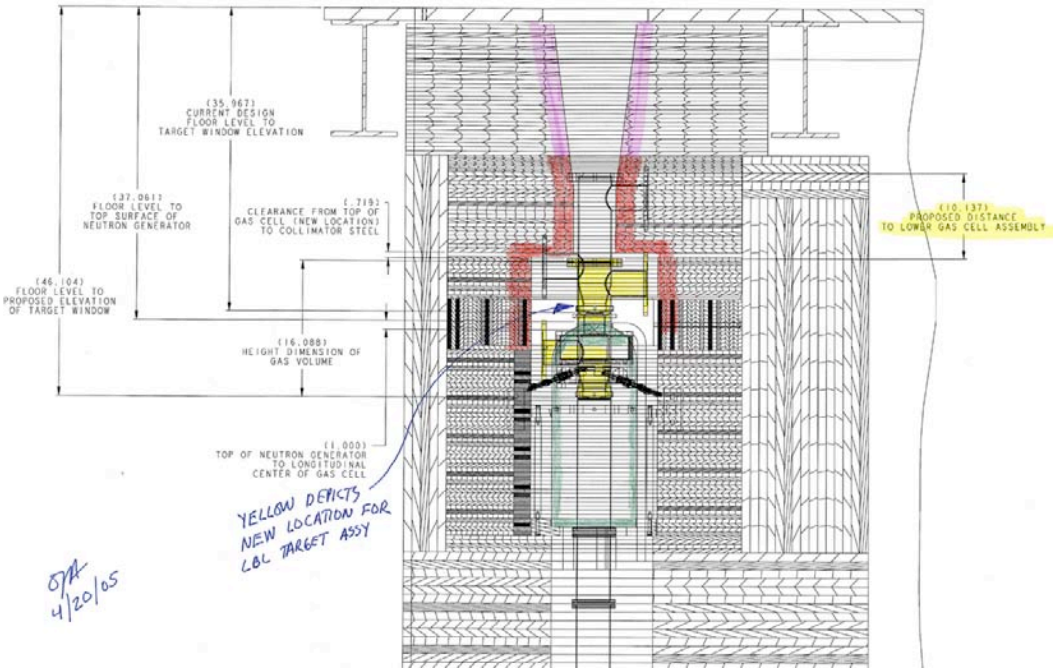

Figure 3.3-3 Collimator dimensions.

The collimator shown above has been used to define an interrogation beam that is approximately 1.3 m wide at the cargo centerline and is thus fairly well matched to the diffusion width of the beam described above. At the same time the collimation angle is narrow enough to provide low personnel exposure in the experiment zone around the neutron source.

3.4 Summary of neutron source characteristics

Table 3.4-1 Neutron source parameters

Parameter	Optimal value	Comments
Neutron energy (MeV)	7	Low end is adequate
Deuteron energy (MeV)	4	Low end is adequate
Peak beam current (mA)	$\geq$ 0.6-1.4	Depends on irradiation length, beam duty factor
Pulse format (s)	1-30	
Collimation ($\Delta\theta$ degrees)	$\geq$ 15	Driven by personnel dose

3.5 Detection of delayed γ-radiation

3.5.1 Detector type

There are more than 1000 γ-ray lines in fission product β-decay above $E_\gamma \geq 3$ MeV. Measurements confirm that the emission spectrum is extremely complex with very little of the total intensity presenting itself in lines that stand out above the continuum[1]. Consequently, high spectral resolution in the γ-ray detector has little useful value and the primary requirement focuses on detection efficiency at high energy. Appropriate high-energy γ-ray spectrometers include liquid scintillators, plastic scintillators, BGO or NaI(Tl) scintillators, and high-pressure Xe proportional counters. In the work reported here proportional counters were eliminated due to their inadequate efficiency. BGO and NaI scintillators were eliminated due to their high cost for a given detection efficiency and the latter was eliminated due to its susceptibility to activation during the neutron irradiation. While activation does not cause a problem in applications such as PFNA where the γ-ray detection window is a very narrow time gate immediately following the beam pulse, β–delayed radiation detection obviates the time window and activation is a major problem. Thus the primary detector studies in this work dealt with liquid and plastic scintillators.

3.5.1.1 Liquid scintillators

Large lucite tubes were filled with xylene-based liquid scintillator. The tubes had diameter D=20 cm and length L=200 cm. A large (D= 20 cm) PMT was coupled directly to the liquid at each end and four tubes were assembled into a detector module as shown below.

Figure 3.5.1.1-1 Liquid scintillator array

The two PMT outputs for each tube were summed electronically and the sum pulse was recorded as a pulse height spectrum. An example is shown below.

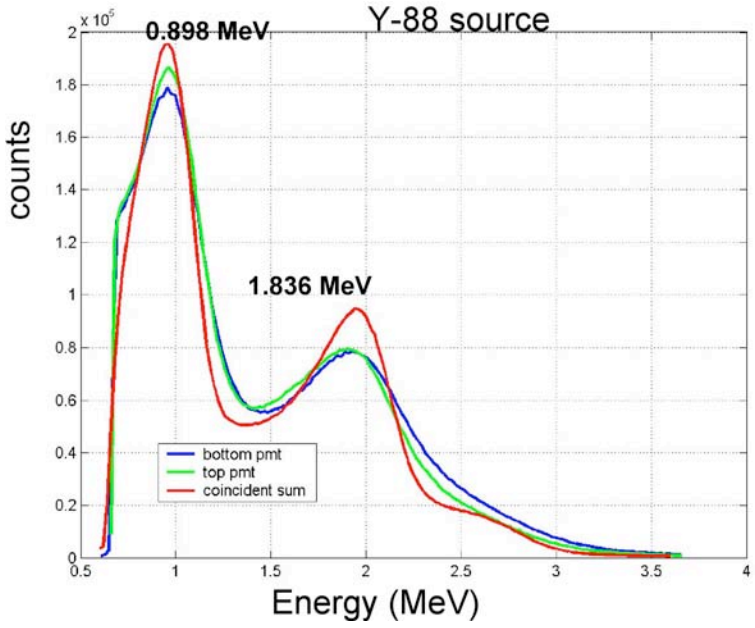

Figure 3.5.1.1-2 Pulse height spectrum for liquid scintillator exposed to ^{88}Y.

Note that there is negligible photoelectric or pair production interaction in a low–Z detector such as a liquid scintillator. The interactions are almost entirely due

to Compton scattering. However, the detector is thick enough, i.e. several mean free paths even at E_γ=3-4 MeV so that multiple Compton scattering events that deposit a large fraction of the γ-ray energy to produce a peak in the pulse height spectrum that resembles a classic full energy peak, albeit one with poor energy resolution. Energy resolution observed is typically on the order of $\Delta E/E \sim 25\%$ (FWHM) at E_γ=662 keV and 13% at E_γ=6.1 MeV.

Liquid scintillation detectors can be constructed inexpensively in a wide variety of configurations and thickness. The medium is relatively clear with long optical mean free path so that pulse height resolution is often superior to that of plastic scintillators. However, maintenance was found to be difficult and expensive due the tendency of the solvents in the scintillator to dissolve the glue used to seal the PMTs. Leakage of the scintillator and needed catch basins made these detectors problematic in usage and were ultimately judged not optimal for a field application. Routine filtering of the liquid to maintain clarity is also an expensive maintenance burden.

3.5.1.2 Plastic scintillators

Plastic scintillators are available in a wide range of sizes up to 122 cm long and 25 cm thick. PMTs may be coupled onto any surface and multiple PMTs may be employed. These configurations are slightly more expensive than their liquid scintillator counterparts but they do not require the auxiliary liquid purification systems or the catch basins that capture a spill from leaks or breakage. Overall system cost is relatively small and comparable to the liquid scintillator configurations.

Several plastic scintillator formats have been studied in detail and they are shown schematically below.

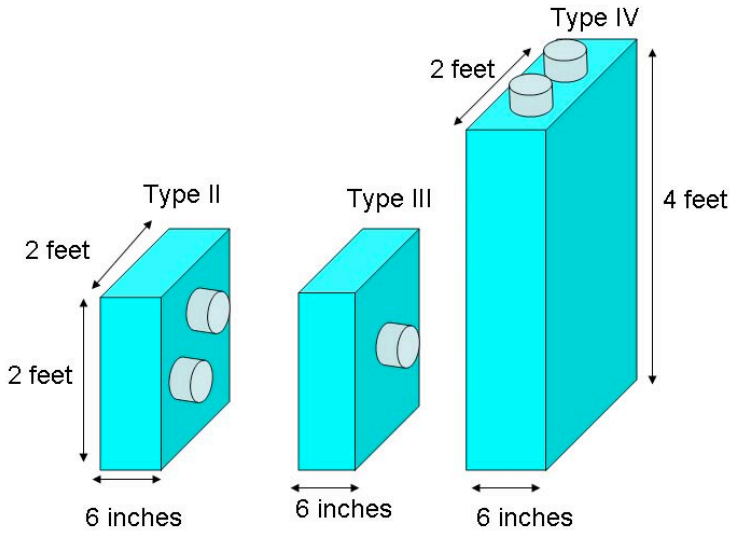

Figure 3.5.1.2-1 Plastic scintillator geometry

Scintillators of thickness L=15 cm and L=25 cm were compared. Lateral dimensions 61 cm X 61 cm and 61 cm X 122 cm were compared. Detectors with a single PMT on the lateral surface and with two PMTs on the lateral surface were compared with each other and with configurations where two PMTs were coupled onto the end of the detector. An example of one deployed detector configuration is shown below.

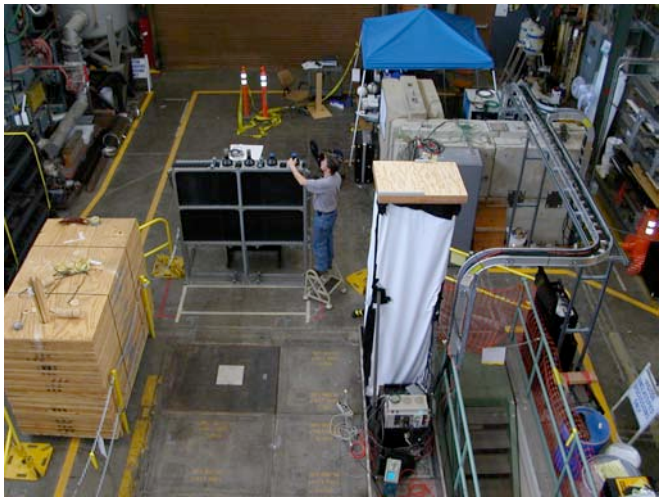

Figure 3.5.1.2-2 Deployed array of plastic scintillators. Right hand photo shows an L=25 cm thick array on the right and an L=15 cm thick array on the left.

In the configuration shown a 61 cm X 122 cm detector is placed alongside a stacked pair of 61 cm X 61 cm detectors. The former has PMTs on the top edge and the latter have PMTs on the larger lateral surface on the backside, hidden from view. The PMTs are visible in the pictures.

The plastic arrays have been characterized with regard to pulse height resolution. Typical results are shown below for a collimated source located near the center of the lateral detector face. One detector had a single PMT on the lateral face while others had two PMTs whose signal outputs were summed. For comparison the pulse height spectrum for a liquid scintillator tube is shown where two PMTs were coupled on the end and their outputs summed. Examination of the figure shows that the liquid scintillator has superior resolution and the single PMT 61 cm X 61 cm detector has poorer resolution by a factor of ~ 1.5.

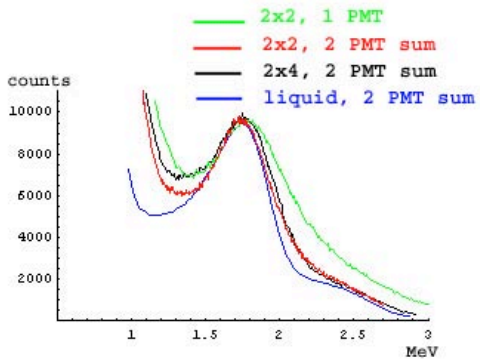

Figure 3.5.1.2-3 A comparison of the resolution for the 4 different cell types.

The resolution is defined as the width of a Gaussian function fit to the upper lobe of the approximate 1.836 MeV peak induced by ^{88}Y. An indication of the sum peak is visible in the liquid energy spectrum. The energy resolution obtained in these measurements is summarized in the table below.

Table 3.5.1.2-1 The effective energy resolution of four different cell types.

Cell Type	Mean energy (MeV) from Gaussian fit to background subtracted peak	FWHM (= 2.35σ with σ from Gaussian fit to background subtracted peak)
I- Liquid 2 PMT summed	1.78	33%
II- 61x61 cm, 2 PMT summed	1.87	34%
III – 61x61 cm, 1 PMT	1.82	50%
IV- 61x122 cm, 2 PMT summed	1.78	42%

In summary, for a 25 cm depth of plastic scintillator with unit density:

- At least 35% of 6 MeV photons will deposit > 3 MeV in the detector.
- At least 26% of 4 MeV photons will deposit > 3 MeV.
- At least 30% of 3 MeV photons will deposit >2 MeV.

And the energy resolution is in the range 10-50%. This resolution, while not good for spectroscopy measurements, is adequate for discrimination of high-energy fission product radiation from terrestrial background radiation.

Finally, low energy background radiation is readily discriminated from the signal of interest but does contribute to a very large count rate in such highly efficient detectors. It is thus beneficial to wrap the detectors in a lead shield to suppress the unintended count rate due to low energy γ-radiation. The arrays

used in the system described here had a single sheet of 3.2 mm thickness lead covering the face toward the cargo. The results are shown in the figure below.

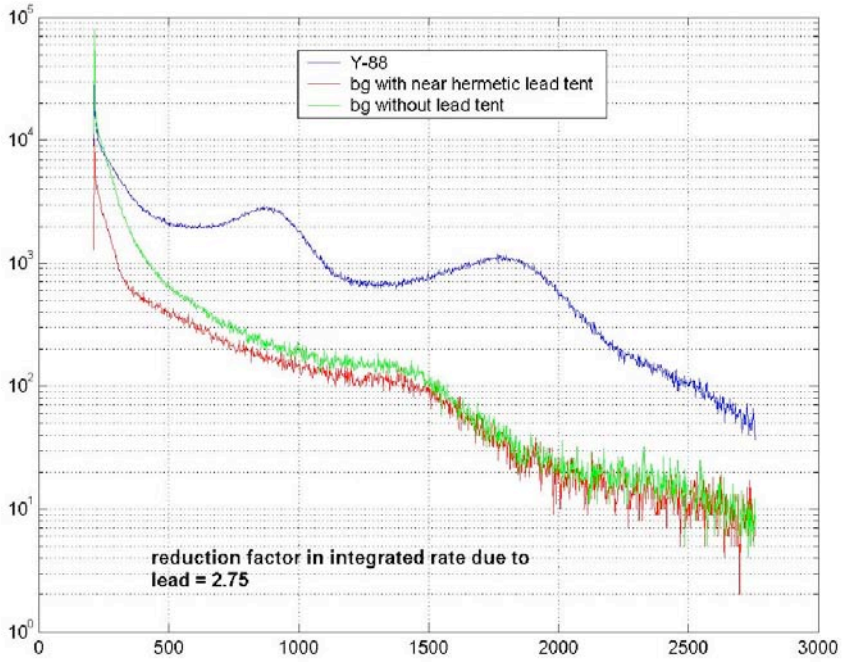

Figure 3.5.1.2-4 The effect of a near-hermetic lead blanket on the background spectrum in a 1-foot x 1-foot plastic scintillator detector.

The integrated rate is reduced by a factor of 2.8. The small thickness of lead utilized to suppress low energy events is essentially transparent to the high-energy radiation that makes up the SNM signal. This is a significant improvement in performance over the unwrapped detector.

3.5.2 Detector energy threshold for delayed γ-radiation

Improved SNM detection is obtained by setting an energy threshold in the γ-ray detection system that makes the detectors nearly blind to terrestrial background radiation and nearly blind to most activation products generated during the interrogation. Detailed studies of performance obtained at various energy thresholds have not been completed at the time of this report and will be the subject of another report. It is known that there are very few neutron-induced activation products that produce γ-radiation above 3 MeV and nearly all of those have half-lives much longer than fission products, i.e. $T_{½} >> 1$ min. Decay scheme data found in the published literature[15] has been used to identify species that could possibly interfere with fission product detection or generate false positive identification of SNM and those were summarized in Table 3.1.3-2.

There are relatively few activation products capable of generating interference radiation. When the neutron energy is $E_n \leq 10$ MeV the only target species with high specific activity is ^{19}F. The others have specific activity 3-5 decades less than

does ^{19}F and are of much less concern. Preliminary analysis of activation data indicates that an $E_\gamma \geq 3$ MeV threshold excludes all but steel activation and that is a fairly minor contributor. When the threshold is lowered to $E_\gamma \geq 2$ MeV interference due to activation of cargo and container components becomes important. This is seen in the two figures below where the one on the top employs the 3 MeV threshold while the one on the bottom employs a 2 MeV threshold.

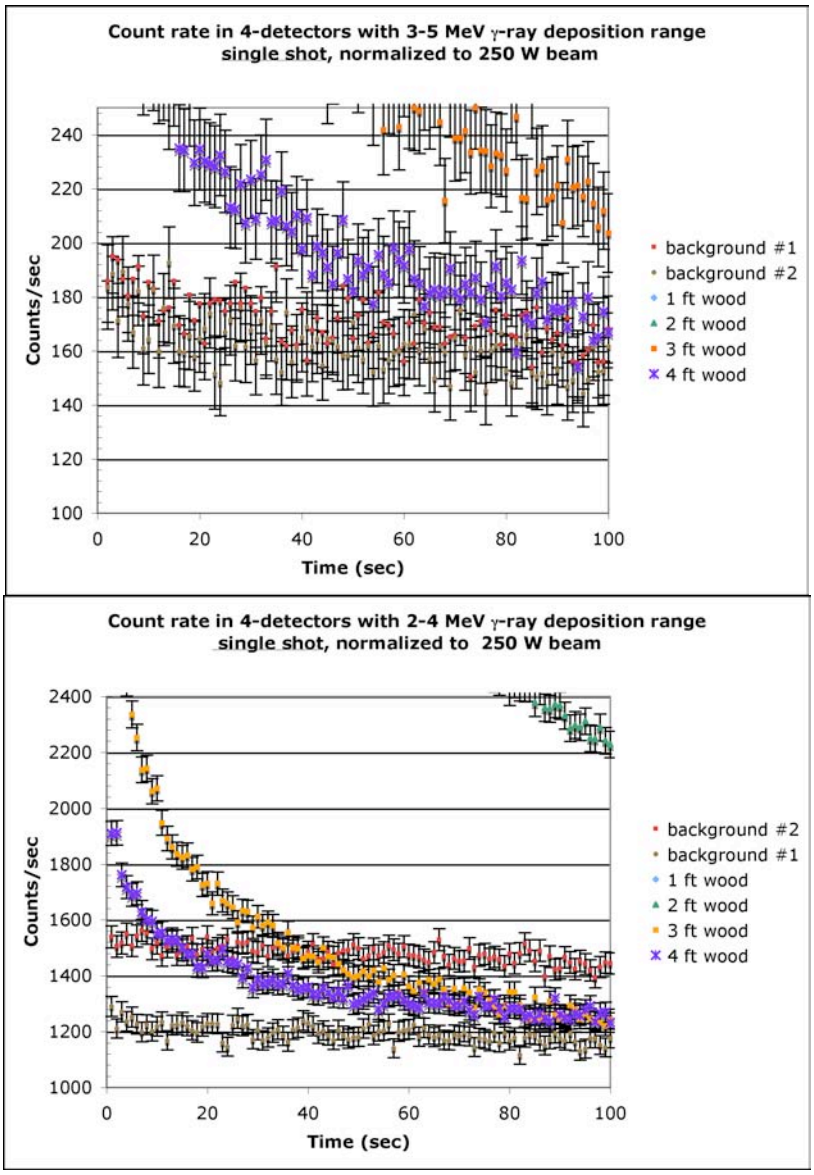

Figure 3.5.2-2 Decay curves for two distinct γ-ray energy thresholds. a) $E_\gamma \geq 3$ MeV, b) $E_\gamma \geq 2$ MeV.

It is important to notice the background decay curves at both threshold values. They are indicated by the red and brown dots in both figures where red dots correspond to a measurement immediately after irradiation and brown just before irradiation but where a previous irradiation was imposed a few minutes

earlier. Both data sets show a very small amount of short-lived activity in the background but the level is small compared to the signal data. Changing the energy threshold for detection has a very slight impact indicating that the background species has a fairly high energy. However, data in the lower figure shows a significant count rate due to long-lived background due to induced radioactivity (red) that is rejected at the higher detection threshold value. The normal background due to cosmic radiation is indicated by the brown data points and its level depends on the detection threshold set. This suggests that the lower threshold is low enough to admit a small amount of activation interference, though the detected activity is long-lived and can be distinguished by this characteristic. Overall, this highlights the need to set a suitably high γ-ray energy threshold as a means of reducing the need for frequent background measurements and unneeded complexity

3.5.3 Detector configuration

No detailed studies were carried out to optimize the placement of detectors. Ideally the interrogated cargo zone would be surrounded by detectors on all sides to maximize detection efficiency and reduce the interrogation dose needed to provide adequate sensitivity. At the very least a band of detector arrays on two sides and the top of the cargo container and extending along its length to an extent L = ±100 cm would be prudent and not prohibitively expensive.

3.5.4 Optimum detectors

Plastic scintillation detectors have proven best for detection of high-energy γ-radiation. Increasing thickness up to L=25 cm improves both the detection efficiency and the energy resolution. The improved resolution results from a larger number of detected events that interact two or more times to deposit nearly the full γ-ray energy in the scintillator. Large detector dimensions up to 61 cm width will, with proper dielectric coating for good reflection, provide spatially uniform light collection and thus adequate energy resolution. Good performance has been obtained with a single D=13 cm PMT on the rear surface. Arrays can readily be constructed from blocks of 61 cm X 61 cm X 25 cm plastic detectors stacked vertically and arrayed horizontally.

3.6 Detection of delayed neutrons

Delayed neutrons are produced at ~ 1/10 the rate of high energy delayed γ–rays[5]. They are strongly attenuated in hydrogenous cargos so that this signature is not robust for agricultural, textile, liquid, or fuel cargos. Nevertheless, metal cargos including steel, copper, cable spools, power transformers, and machinery are nearly transparent to the interrogation beam and to the emitted β-delayed neutrons. Therefore it is efficacious to augment high-energy γ-ray detection with a means to detect delayed neutrons.

One of the most commonly used and robust means of detecting low energy neutrons in the field is a polyethylene-moderated array of ^{3}He proportional counters. These detectors normally consist of ^{3}He tubes of 5-8 cm diameter and

60-180 cm length, and they are filled to 2-5 atm ^{3}He. Arrays typically have 2-10 modules, each containing 4-8 tubes embedded in a block of polyethylene of thickness 5-10 cm. These detectors are appropriate for the cargo scanning application presented here and have been found to be reliable and robust in the field. An example of the delayed neutron signal detected with steel cargo is shown in the figure below.

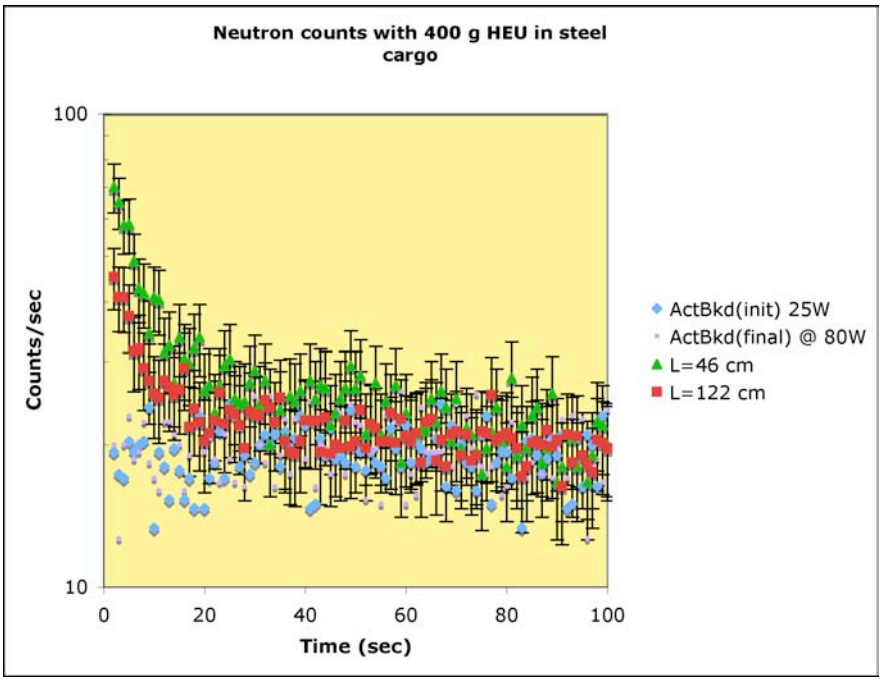

Figure 3.6-1 Delayed neutron count rate data for steel cargo L=40-122 cm thick and mean density <ρ> = 0.6 g/cm3. Data shown is for 400 g HEU sample [6].

3.7 Timing of the irradiation and counting

During an irradiation the fission product precursors are generated at a rate P and the average of their mean lifetimes for decay is $\tau=1/\lambda$. If the irradiation has duration T and subsequent counting of the high energy γ-radiation continues for time t-T after the end of the irradiation so that the full cycle completes in time t, then the total decays to be detected is given by the following relation[5].

$$C = \frac{P}{\lambda}\left(1-e^{-\lambda T}\right)\left(1-e^{-\lambda(t-T)}\right) \qquad 3.7\text{-}1$$

It is easily shown that the greatest number of decays will occur during the counting interval when (t-T)=T, that is when the duty cycle is 50% and T=t/2. High-energy γ-radiation is produced by a number of fission products with various decay times. However, the total count rate observed due to high-energy γ-radiation is reasonably well described by a small number of decay times[1] with the principal component exhibiting $T_{1/2}$ ~ 22 sec. The optimal irradiation

and counting time for this application is then T=20 sec irradiation and the subsequent counting time (t-T)=20 sec. The overall interrogation time is then t=40 sec.

4. Detection sensitivity of laboratory prototype

4.1 Wood cargo

A disk of HEU in the form U_3O_8 (ρ=2.5 g/cm^3) and containing 376 g ^{235}U was placed at various depths in a stack of plywood (ρ=0.58 g/cm^3). An array of four 25 cm thick plastic scintillation detectors was placed along the side of the stack as shown in the figure below. The array had cross sectional area 121cm X 121 cm and was located ~ 15 cm away from the side of the stack. Two ^{3}He arrays were placed on top of the stack, each contained 8 tubes (5.1 cm diameter X 61 cm length at ^{3}He pressure 4 atm) embedded in 10 cm thick polyethylene.

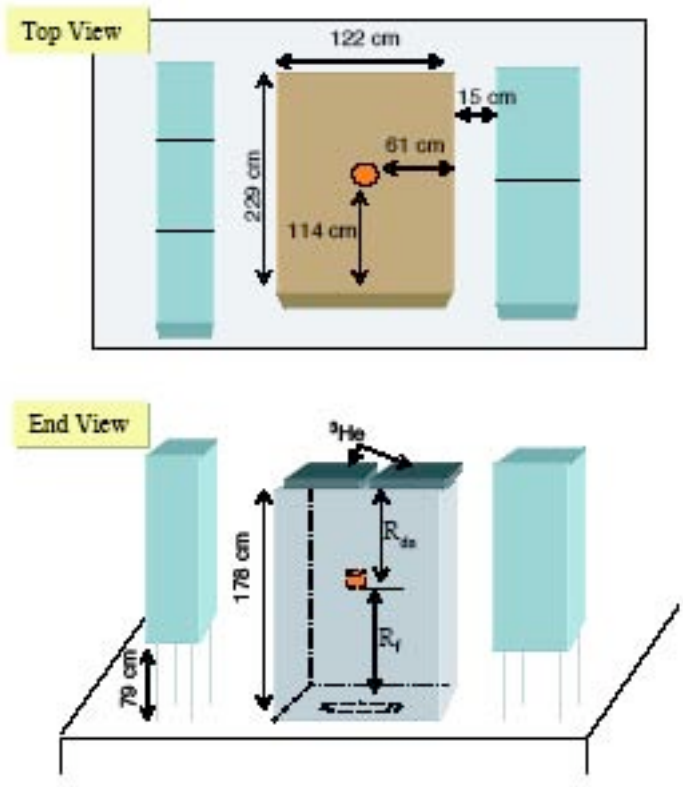

Figure 4.1-1 experimental configurations for HEU sensitivity measurements.

The neutron beam was directed from the floor into the assembly and the beam was on for T=30 sec. Counting in both the ^{3}He array and scintillator arrays accumulated data from the end of the neutron irradiation for a total of 100 sec, i.e. t=130 sec.

No neutron data was recorded for the wood cargo since attenuation essentially eliminates this signal with hydrogenous material in place. The γ-radiation was counted and the results are shown below where the count rate is observed with an energy discrimination threshold $E_\gamma \geq 3$ MeV. More details are available elsewhere[6].

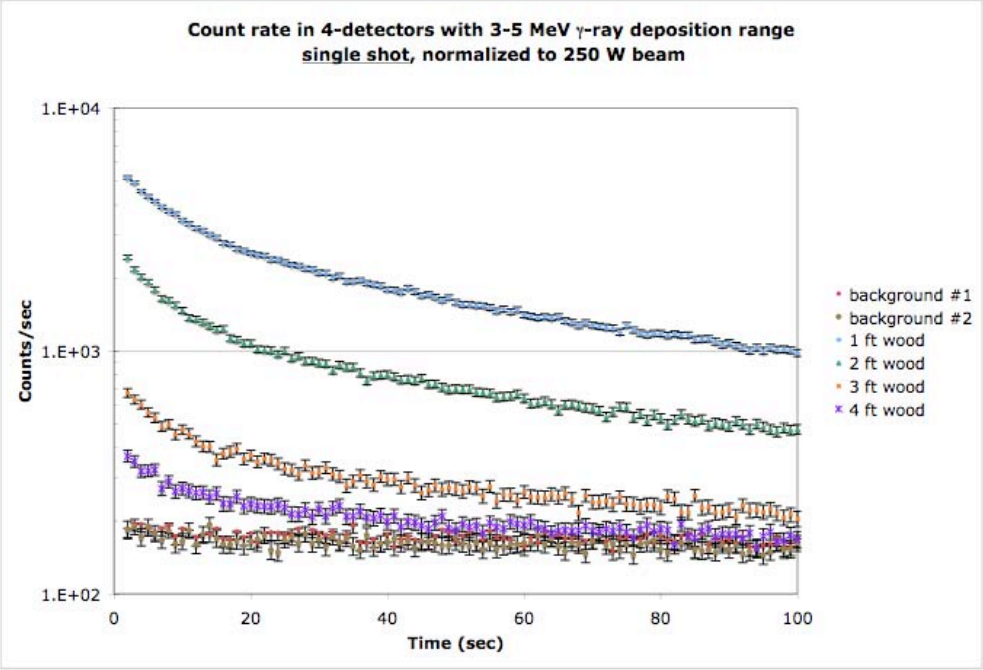

Figure 4.1-2 Count rate in the scintillator array following t=30 sec irradiation. Data are shown for several cargo path lengths above the neutron source[6].

Data shown in the figure shows the "active background" at the bottom. This is the post-irradiation count rate when no HEU is present. The upper two curves show data employing only an m=250 g HEU target at distances 1 ft and 2 ft. The second and third curve from the bottom is for m=376 g HEU located 3 ft and 4 ft above the bottom of the cargo. In all cases the deuteron beam current I_d~50–55 μA.

Error bars shown in the curves are $\Delta C = 2\sigma$, i.e. twice the Poisson estimate. Clearly, the fission product signal is robust and statistically significant even at the deepest burial. That is important since the target sample is very small compared to the goal quantity (m=5 kg) and the beam current is low.

4.2 Steel cargo

The plywood cargo was replaced by a stack of steel pipes $<\rho>=0.6$ g/cm^3 and the measurements repeated. In this case both delayed γ-radiation and delayed neutrons were observed. The results for neutrons were shown in Figure 3.6-1 and are repeated again here with the comparison of neutron and γ-ray count rates.

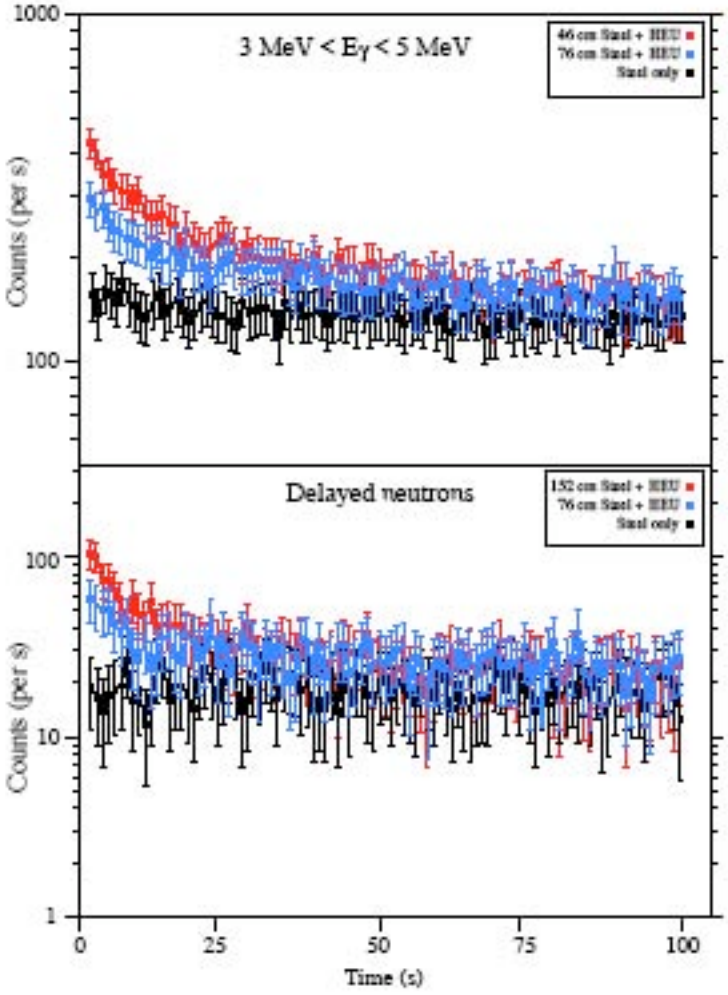

Figure 4.2-1 Delayed neutron and high-energy γ-ray data taken with steel cargo in place[6].

The HEU target was embedded at two locations as indicated in the figure. It is important to note that the geometry of this experiment reduces the distance from source to neutron detector as the SNM target is moved away from the source. The distance from the γ-ray detector is unchanged as the target moves. As before the lowest curve shows the "active background", i.e. the post-irradiation count rate with no HEU present. It is also important to note that consideration of

personnel radiation dose limited the beam current during the steel cargo measurements to $I_d \leq 25$ μA.

Again a robust, statistically significant signal is observed at all depths for both the neutron and γ-ray data channels. Here too the error bars are $\Delta C = 2\sigma$. Even in the case of thick steel cargo the delayed high-energy γ-ray signal produces count rates much higher than delayed neutron signals, and the statistics are better for the γ-ray signal.

There is a suggestion of short-lived steel activation in the "active background" so that there may be at least one short-lived activation product emitting γ-radiation at $E_\gamma \geq 3$ MeV.

4.3 Significance of the measured data

The count rate data shown in the previous section was accumulated for 30 sec after the end of irradiation and the background subtracted from it to obtain an estimate of the signal. Results are shown in the table below.

Table 4.3-1 Experimental results with wood and steel cargo

Signal	Cargo	^{235}U mass (g)	Depth of target R_f(cm)	Cargo ρL, (g/cm^2)	Signal counts, S	Background standard deviation, σ	$F_s=S/\sigma$
3-4 MeV γ	Wood	221	30	17	29,000	186	160
"	"	"	61	35	12,700	189	67
"	"	376	91	53	3717	167	22
"	"	"	122	71	2306	171	14
3-4 MeV γ	Steel	"	46	28	7995	543	15
3-5 MeV γ	"	"	76	46	6389	483	13
"	"	"	122	73	6668	538	12
Delayed neutron	"	"	46	28	1326	96	14
"	Moderator added	"	76	46	1042	90	12
"	"	"	122	73	1258	140	9

Entries in the table include the estimated σ due to random run-to-run variations in the "active background" and these estimates are generally larger than the Poisson estimate. In the case of steel cargo the interference due to activation increases σ substantially.

It was shown earlier that those threats where $F_s \geq 4$ are the cases where predicted performance is excellent with low error rates. For $F_s \geq 5$ extremely low error rates

are predicted. All of the above cases with cargo areal density $\rho L \leq 75$ g/cm^2 cargo thickness show $F_s \geq 9$ and thus the results above project to very low system error rates. The low error rates predicted are obtained with very low beam current and short interrogation times, i.e. T=30 sec irradiation and (t-T)=30 sec counting for a total scan time of only one minute; and with target mass of SNM $m \leq 400$ g.

4.4 Projection to field performance

Experimental measurements and validation have been limited to a neutron beam energy $E_n \leq 7$ MeV, beam current $I_d \leq 65$ μA, and typically only four detectors. The SNM targets were limited to $m \leq 400$ g HEU. The results shown in Table 4.3–1 would indicate that the system evaluated in this report is capable of extraordinarily low error rates even with SNM targets much smaller than the goal quantities, low beam current, and short inspection times utilized in the studies reported earlier. Application to primary screening requires low rates of false positives and extremely low rates of false negatives. Application to secondary screening, i.e. resolving alarms, requires even lower error rates but there is additional tolerance for higher radiation dose and longer interrogation times.

The goals were met even with the smaller prototype when the cargo thickness was limited to $\rho L \leq 75$ g/cm^2. This thickness corresponds to the distance from sidewall to centerline of a cargo container (L=4 ft) when the container is loaded at the maximum density allowed by the container weight limit, i.e. $\rho \leq 0.6$ g/cm^3. This would allow adequate performance on threats containing an SNM target anywhere so long as the container is interrogated from both sides as part of the scan. However, some environments or CONOPS may prohibit scanning from both sides. In this latter case it is necessary to have reliable detection through thicker cargo, even up to $\rho L \leq 150$ g/cm^2. The thicker cargo has not been explicitly addressed in the measurements reported here. Instead an attempt is made to project the performance of an enhanced system where the additional cargo thickness imposes approximately 100X additional attenuation on the interrogation beam for hydrogenous cargo and significant attenuation on the exiting γ-radiation and delayed neutron signals.

The major parameters of the system described above can be enhanced for field applications with corresponding enhancements of system performance. Each parameter change leads to an expected performance improvement scale factor and those scale factors are summarized in Table 4.4-1 below.

The previous section indicated that project goals are met at beam currents as low as $I_d \geq 15$ μA. Beam currents in commercially available accelerators can be more than $I_d = 400$ μA and possibly as high as $I_d = 1.5$ mA. Background variations are weakly sensitive to neutron intensity while signal strength, S, is directly proportional to beam intensity. Thus a 30X-100X increase in beam current is expected to increase F_s by nearly as large a factor.

The goal quantity of SNM was a 5 kg solid sphere of ^{235}U metal. Simulations show that the fission product signal is ~ 3X higher for 5 kg in steel cargo compared to the 376 g target used in the experimental evaluations. The increase is limited by the deep penetration of the unmoderated neutrons into the SNM and consequent strong attenuation of the fission product γ-radiation within the SNM target. On the other hand wood cargo produces a highly thermalized neutron spectrum that does not penetrate the SNM target more than 1-2 mm and the fission rate is high only at the surface. The γ-ray attenuation is consequently small but the effective volume of the SNM exposed to the neutron flux is a good deal less than the total volume. The 5 kg solid sphere in wood is predicted to produce 5X higher signal output than the 376 g sample tested in the experiments. Overall, we conclude that the goal quantity SNM target produces 3X-5X higher signal than the target on which measurements were made.

It was shown earlier that increasing the interrogation beam energy from En=7 MeV to En=10 MeV improves the beam penetration due to a ~ 20% reduction in attenuation coefficient. The net effect depends on the type and thickness of cargo. Monte Carlo simulations generally showed a ~ 2X increase in fission rate when the beam energy was increased in this range. In the analysis presented here it was determined that this increase is not cost effective and not optimal.

Increasing beam current produces a proportional increase in detected signal. However, it also generates additional interference intensity and thus larger variance in background levels. The latter effect produces background/interference that reduce the figure of merit roughly as the square root of beam intensity so that the net enhancement in our figure of merit is on the order of 10X when the beam is increased 100X.

Operational limits may require high velocity as the cargo passes through the portal, thus reducing the irradiation time, T, compared to the experimental evaluations. The net effect of limiting the scan to one minute total irradiation plus counting time will reduce the mean irradiation to T~ 2.5 sec or 0.08X. However, this has the same effect on activation background as a reduction in beam current and thus affects the figure of merit only as the square root, i.e. a net reduction in performance of 0.29X.

Finally, the detector efficiency can be increased by employing additional detectors, up to four times as many, for a 16X improvement in detection. Here too, the corresponding increase in background offsets this by the square root of efficiency so that the net improvement in the figure of merit is 4X

The projected improvements in performance when the system is upgraded to field-scale parameters are summarized in the table below. If all of these improvements are invoked then there is a potential increase in performance up to 35-60X when compared to the experimental data reported with the limited interrogation system employed for assessments.

Table 4.4-1 Performance improvement factors

POC parameter value	Enhanced value	Parameter increase	Performance increase in F_s
Goal quantity, m=376 g	M= 5 kg	13X	3X-5X
Beam current, I_d=15 μA	I_d=1500 μA	100X	10X
Neutron pulse duration, T=30 sec	T= 2.5 sec	0.08X	0.29X
Detector efficiency, Aε=4500 cm^2	Aε=71,000 cm^2	16	4X
Overall potential enhancement			35-60X

The measurements described above were confined to areal density in the range $\rho L \leq 75$ g/cm^2. Most normal cargos[13] have density $\rho \leq 0.3$-0.4 and so the areal density looking through cargo from the wall to the centerline is $\rho L \leq 35$-47 g/cm^2 and the system evaluated above seems to meet the goals even when scan time is limited to t=60 sec and the goal quantity is m ≤ 400 g HEU. On the other hand, if the CONOPS prohibits inspection from both sides of the container, scanning only from one side, then it is necessary to penetrate, vertically or horizontally, through $\rho L \leq 75$-150 g/cm^2. At the high end of this range the additional attenuation of the interrogating beam in hydrogenous cargo could be up to two decades and then it would be necessary to invoke all of the enhancements listed in the table above.

Application of this technique to secondary screening for the purpose of resolving alarms generated by primary screening changes the demands significantly. Many of the cargos likely to generate concern in primary screening will be those with density higher than usual, with substantial masses of high-Z material, or extensive clutter due to highly heterogeneous loading. In this case there may be substantial lumps in the cargo with density larger than the average for the container or the average for normal flow of commerce. In short, it may be important to attain low error rates at unusually high density so that the range of interest may extend up to $\rho \leq 2$ g/cm^3 over pallet sized volumes and thus areal density may have to extend to $\rho L \leq 200$ g/cm^2. No measurements or simulations have been carried out for this case. However, both measurements and simulations indicate that an additional thickness of cargo ρL=100 g/cm^2 results

in roughly 100X additional attenuation of the primary beam if it is necessary to detect all threats from one side of the container. Thus, if it is necessary to detect SNM not up to the container centerline but, instead, on the opposite side of the container then a two-sided scanning system may be required with irradiations from both sides. This could be accomplished with dual neutron sources or by executing two serial scans, one from each side over an extended time period.

If it becomes necessary to carry out the detection employing irradiation from only one side and without repeating the scan from the other side, then additional 100X attenuation must be accommodated. In this case all of the system enhancements described earlier must be invoked. The important thing to note is that those enhancements are available utilizing commercially available components and performance is expected to be satisfactory.

5. Conclusion

Table 4.4-1 summarizes optimal parameters of a neutron interrogation system for reliable detection of SNM. A goal has been set for resolving alarms generated when primary screening of maritime cargo containers indicates the possibility of SNM being present, hidden in the cargo. That goal was $P_d \geq 95$ % detection probability and $P_{fA} \leq 0.001$ false positive rate for an m=5 kg solid sphere of ^{235}U embedded in the cargo. Specific cargos of interest to represent the most challenging cases of normal commercial traffic included fully loaded containers of steel or wood. The maximum cargo thickness, 8 ft, combined with the highest mean density limited by the container weight limit, 0.6 g/cm^3, establishes the most challenging cargo threat for single-side scanning as $\rho L \leq 150$ g/cm^2 or for two sided scanning $\rho L \leq 75$ g/cm^2. The proposed screening concept was based on neutron interrogation to generate fission in the hidden SNM followed by detection of delayed neutrons and delayed high-energy γ-radiation.

Analysis of simulations and experimental data indicate the optimal neutron interrogation energy to be E_n=7-9 MeV with the neutrons generated by the D(d,n) reaction in a gas D_2 target where the deuteron beam energy is E_d=4-6 MeV. A source at the low end of this range is adequate to meet the goals for two-sided interrogation at $I_d \geq 15$ μA or for single-sided interrogation at $I_d \geq 1.5$ mA. At the lower end of the neutron energy range target yield is lower by ~ 2X and the induced fission rate per neutron is reduced ~ 2X so that 4X higher beam current is required. A cost/efficacy tradeoff can then be made where the smaller footprint of the lower energy machine is compared to the cost advantages and liabilities of the higher energy machine.

Given the extraordinarily large number of unresolved γ-ray lines the optimal detector for the γ-radiation is a low-resolution scintillator such as a large plastic block. Adequate performance is obtained from low-cost plastic scintillators of 25 cm thickness and large cross sectional areas up to A=15000 cm^2 and the best tradeoff between detection sensitivity and background rejection requires an energy discriminator at $E_{min} = 3$ MeV. For the delayed neutrons the optimal detector is a moderated ^{3}He array.

The fission product signal has several decay times but the bulk of the γ-radiation can be described by a half-life $T_{½}$ ~ 22 sec so that the optimal irradiation time is T=20-30 sec and the optimal counting time is the same. Consequently, a t~ 40–60 sec interrogation time provides the greatest sensitivity with the beam on half of that time.

An interrogation system operated near these optimal parameter values is shown to meet the detection and false alarm goals for the intended SNM target. There are several options for changing the CONOPS, such as two-sided scanning, to accommodate threats more challenging than those considered here. Also, the beam current could be increased above the range considered here so that the technique is robust in its ability to provide adequate performance in the most challenging threat scenarios and the most rapid scanning or alarm resolution. The previous sections establish the optimal design parameters and project fully adequate SNM detection performance even in the most challenging threat scenarios. Experimental data supports the signal level estimates and provides reliable background estimates. The experimental assessments have been comprehensive and exposed no serious shortcomings and no serious error rates.

6. Bibliography

1 E. B. Norman, S. G. Prussin, R.-M. Larimer, et al., "Signatures of special nuclear material: High-energy γ-rays following fission", Nuclear Instruments & Methods in Physics Research A **521/2**, 608 (2004).

2 D. R. Slaughter, M. R. Accatino, A. Bernstein, et al., "The nuclear car wash: A system to detect nuclear weapons in commercial cargo shipments", Nuclear Instruments and Methods B (2006).

3 D. R. Slaughter, M. R. Accatino, A. Bernstein, et al., "The "nuclear car wash": a scanner to detect illicit special nuclear material in cargo containers", IEEE Sensors Journal **5**, 560 (2005).

4 D. R. Slaughter, M. R. Accatino, A. Bernstein, et al., "Preliminary results utilizing high-energy fission product γ-rays to detect fissionable material in cargo", Nuclear Instruments and Methods B **241**, 777 (2005).

5 D. Slaughter, M. Accatino, A. Bernstein, et al., "Detection of special nuclear material in cargo containers using neutron interrogation", UCRL-ID 155315, Lawrence Livermore National Laboratory, Livermore, CA, August, 2003,

6 J. Church, A. Bernstein, M.-A. Descalle, et al., "Study of signal interferences in the nuclear car wash", Nuclear Instruments & Methods in Physics Research A **this proceedings** (2006).

7 G. R. Keepin, "Nuclear safeguards research and development", LA 4368-MS, Los Alamos National Laboratory, Los Alamos, NM, October-December, 1969,

8 G. R. Keepin, "Nuclear safeguards research and development", LA- 4457-MS, Los Alamos National Laboratory, Los Alamos, NM, January-April, 1970,

9 C. E. Moss, C. L. Hollas, G. W. McKinney, et al., "Comparison of active interrogation techniques", 2005, IEEE Nuclear Science Symposium, San Juan, Puerto Rico, 23-29 October, IEEE,

10 J. L. Jones, W. Y. Yoon, D. R. Norman, et al., "Photonuclear-based, nuclear material detection system for cargo containers", Nuclear Instruments and Methods B **241**, 770 (2005).

11 C. E. Moss, M. W. Brener, C. L. Hollas, et al., "Portable active interrogation system", Nuclear Instruments and Methods B **241**, 793 (2005).

12 J. A. Church, D. R. Slaughter, E. B. Norman, et al., "Experimental study of variations in background radiation and the effect on Nuclear Car Wash sensitivity", UCRL-TR Lawrence Livermore National Laboratory, Livermore, CA, 2007,

13 M.-A. Descalle, D. Manatt, and D. Slaughter, "Analysis of recent manifests for goods imported through US ports", UCRL-TR 225708, Lawrence Livermore National Laboratory, Livermore, CA, October 31, 2006,

14 J. M. Hall, S. Asztalos, P. Biltoft, et al., "The nuclear car wash: Neutron interrogation of cargo containers to detect hidden SNM", UCRL-JRNL 225004, Lawrence Livermore National Laboratory, Livermore, CA, October, 2006,

15 LBNL_Nuclear_Science_Division, "Table of Isotopes", 2003, http://ie.lbl.gov/toi/.